Journal of Oceanography, Vol. 63, pp. 77 to 100, 2007

Three Dimensional Diagnostic Modeling Study of the South China Sea Circulation before Onset of Summer Monsoon in 1998

YAOCHU YUAN*, GUANGHONG LIAO and XIAOHUA XU

State Key Laboratory of Satellite Ocean Environment Dynamics, Second Institute of Oceanography, State Oceanic Administration, Hangzhou 310012, P.R. China

(Received 17 April 2006; in revised form 4 August 2006; accepted 7 September 2006)

The wind data from NCEP and hydrographic data obtained from April 22–May 24, 1998 have been used to compute the circulation in the South China Sea (SCS) using three dimensional diagnostic models. The main numerical results with SSHA derived from T/P altimeter are as follows: most of intruded Kuroshio bypasses. However, a part of Kuroshio intrudes westward above 300 m levels. This intruded westward flow is narrowly confined to the continental slope south of China, in agreement with the findings of Qu *et al*. (2000). The basin-scale cyclonic gyre dominates in the northern SCS and consists of two cyclonic eddies, C2 and C3, above 300 m levels. However, it is separated into two parts by an anti-cyclonic eddy, W4, below 300 m. The basin-scale anti-cyclonic gyre dominates in the central SCS and consists of three anti-cyclonic eddies, W1, W2 and W3, above 300 m levels. However, below 300 m it consists of the anti-cyclonic eddies W1, W2 and W4 and extends northward to near 20°N. A northward coastal jet is present near the coast of Vietnam at depths above 300 m, and develops northward further to about a distance of 3°15′ N than that in cruise 2. The most important dynamical mechanism is due to the joint effect of the baroclinity and relief. The second dynamical mechanism is due to the interaction between the wind stress and relief. The topography effect is more important than the ß effect. The Sverdrup relation cannot be satisfied in the SCS.

Keywords:
- SCS circulation,
- before the onset of summer monsoon in 1998,
- three dimensional diagnostic modeling,
- cyclonic and anti-cyclonic eddies,
- basin-scale gyre,
- dynamical causes JEBAR and IBWSR.

1. Introduction

The South China Sea (hereafter referred to as SCS) is the largest marginal sea in Southeast Asia with an area of 3.5×10^6 km^2, and is a nearly-enclosed basin. The deeper channel between the SCS and the Pacific Ocean is the Luzon Strait between Taiwan and Luzon Islands. The monsoon prevails over the SCS. Su (1998, 2004), Su *et al*. (1990), Hu *et al*. (2000) and Yamagata (2001a, b) etc. have reviewed the previous studies on the circulation in the SCS. We do not repeat such a review of the previous studies here, merely summarizing the following three points.

1) Wyrtki (1961) early provided the pattern of circulation in the SCS, which was basically a cyclonic gyre in winter and an anti-cyclonic gyre in summer, as a result of the seasonally reversing monsoon. However, whether winter or summer, the circulation in the SCS is more complex than the pattern of circulation provided by Wyrtki (1961), for example refer to Qu (2000), Chu *et al*. (1999), Huang *et al*. (1994), Takano *et al*. (1998), Liu *et al*. (2000), Yuan *et al*. (2004), Wang *et al*. (2004) etc. This shows that there are some problems that remain unclear, such as what causes the difference between the patterns of circulation obtained by the above different studies, and what dynamical mechanism results in the seasonal and interannual variations of the circulation in the South China Sea (SCS).

2) Water exchange in the Luzon Strait is complex. The annual mean Luzon Strait Transport (LST) obtained from model studies was 2.4 Sv (Qu *et al*., 2004), 6.5 Sv (Chu and Li, 2000) and 2.0 Sv (Xue *et al*., 2004) etc. The model had a representation of the seasonal variation of LST, showing a maximum (6.1 Sv westward) in winter and a minimum (0.9 Sv, eastward) in summer (Qu *et al*., 2004). On an interannual time scale, LST tends to be larger during El Niño years and smaller during La Niña years (Qu *et al*., 2004). Most numerical models of the SCS with open boundaries showed that the intruded Kuroshio forms

* Corresponding author. E-mail: yuanyc2@yahoo.com.cn

an anticyclonic current loop and a branch current (cf. Hu *et al*., 2000; Xue *et al*., 2004). However, Su (2004) and Su *et al*. (1999) explained the discrepancy between the modeled and observed flow patterns, and pointed out that available hydrographic data do not support the notion that the Kuroshio water enters the South China Sea as a "branch" current, nor primarily as meso-scale eddies. Metzger and Hurlburt (2001) emphasized that accurate representation of the small islands and shoals in the Luzon Strait needs a 1/16° resolution or finer. In such a model with 1/16° resolution or finer, the mean pathway of the Kuroshio changes such that it bypasses the SCS rather than intruding deeply into it. With coarse grid models that cannot resolve these topographic features, the Kuroshio will form a loop current inside the SCS, intruding deeply into it. Besides the above numerical studies, Qu *et al*. (2000) studied intrusion of the North Pacific Waters into the SCS using water mass distribution on the basis of historical hydrographic data, and they pointed out that from spring to fall, the intrusion water from the Pacific is narrowly confined to the continental slope south of China; only in winter, when the northeast monsoon becomes fully developed, can it spread in the southern South China Sea.

The above remarks give rise to the following unsolved problem: Does the intruded Kuroshio form an anticyclonic current loop west of the Luzon Strait? The question is unresolved because there are no available hydrographic data and the observed currents can support its existence. For a profound understanding of physical processes of water exchange in the Luzon Strait, especially the studies of their dynamic mechanism, it is very necessary to obtain long-term observed currents and hydrographic data and long-term satellite remote data from the cooperative program in the Luzon Strait in future.

3) Several important features of the SCS are very interesting. For example, Shaw and Chao (1994) pointed out a strong coastal jet present at the western boundary, i.e., a southward coastal jet in winter and a northward coastal jet in summer, and so on. Our problem is to determine whether a strong coastal jet is present near the coast of Vietnam in other seasons. Takano *et al*. (1998) have discussed this problem. We shall also discuss it below.

Hydrographic data were obtained during the following two cruises: one obtained in a cruise of April 22–May 24, 1998 (hereafter called cruise 1, see Fig. 1), while another cruise took place in June 12–July 6, 1998 (hereafter called cruise 2), i.e., before and after the onset of the South China Sea summer monsoon in 1998, respectively. On the basis of the hydrographic data from cruise 1, the circulations in the SCS are computed using the three dimensional diagnostic model (Yuan and He, 1982; Yuan *et al*., 1986, 2004; Yuan and Su, 1988, 1992), which is discussed in detail in Section 2. Section 3 discusses the wind

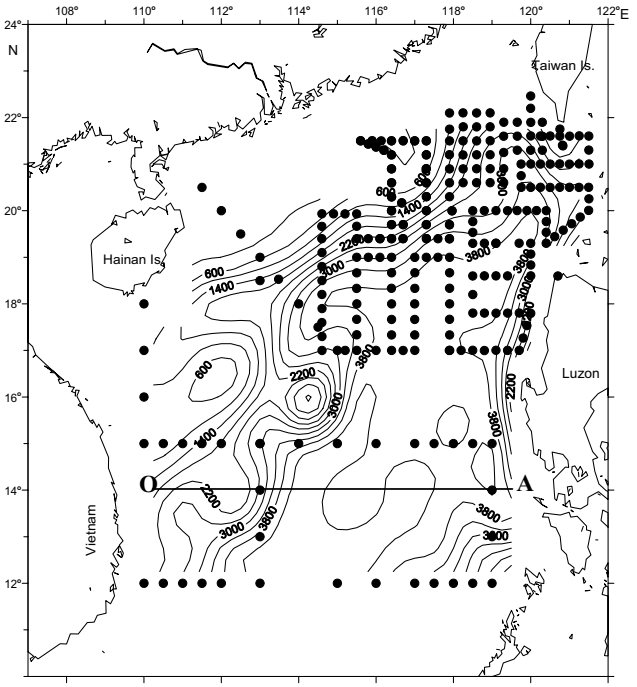

Fig. 1. Location of observed hydrographic stations and bottom topography in the computation region of the South China Sea during April 22–May 24, 1998.

field obtained from NCEP data and the hydrographic analyses and the sea surface height anomaly (SSHA) derived from T/P altimeter data. Section 4 describes the diagnostic computation. A series of numerical experiments are done to select a reasonable value of bottom friction coefficient B. We compute and compare geostrophic and nongeostrophic components of the horizontal velocity vector. Section 5 presents the computational results from cruise 1 according to the three dimensional diagnostic model. We explain the dynamical mechanism that produces the basic pattern of circulation in the SCS. In Section 6 we compare the circulation system in the SCS during cruise 1 with that during cruise 2 (Liao *et al*., 2006) and November 28–December 27 of 1998 (Liao *et al*., 2005). Section 7 presents the conclusion.

2. Governing Equations

We assume that 1) the density field ρ is given from the observed hydrographic data. 2) The wind field over the SCS is obtained from NCEP wind data during cruise 1. 3) The ß effect is considered. As in previous studies (Yuan and He, 1982; Yuan *et al*., 1986; Yuan and Su, 1988, 1992), both the non-linear and lateral friction terms in the momentum equation have been neglected for the circulation in the SCS from the dimensional analysis of the momentum equation. By assuming a constant vertical kinematic eddy viscosity coefficient, A_z, and using a right-

hand Cartesian coordinate system with the z axis directed upward, the steady state momentum and continuity equations are written as follows:

$$f\vec{k}\times\vec{v} = -\frac{1}{\rho_0}\nabla p + \frac{1}{\rho_0}\cdot\frac{\partial\vec{\tau}}{\partial z} \tag{1}$$

$$-\rho g = \frac{\partial p}{\partial z} \tag{2}$$

$$\nabla\cdot\vec{v} + \frac{\partial w}{\partial z} = 0 \tag{3}$$

where the Boussinesq assumption has been made, ρ_0 is a constant reference density, ρ and p are anomalies of density and pressure, respectively, $\vec{v} = (u, \upsilon)$ is the horizontal component of the velocity vector, u and v are the eastward and northward component of the velocity and the other notations are standard, and $\vec{\tau}$ is the friction stress vector:

$$\vec{\tau} = \rho_0 A_z \frac{\partial\vec{v}}{\partial z}. \tag{4}$$

The boundary conditions at the surface are

$$\rho_0 A_z\left(\frac{\partial u}{\partial z}\right)_\varsigma = \tau_x \tag{5.1}$$

$$\rho_0 A_z\left(\frac{\partial \upsilon}{\partial z}\right)_\varsigma = \tau_y \tag{5.2}$$

$$w_\varsigma = 0 \tag{5.3}$$

in which $\vec{\tau}_s$ (τ_x, τ_y) is the wind stress vector and ς is the sea surface elevation. The boundary condition (5.3) indicates that the condition of the "right lid" is satisfied.

The no-slip boundary conditions at the sea bottom with $z = -H$ are

$$u = v = w = 0. \tag{5.4}$$

Vertical integration of the static pressure equation leads to

$$p = \rho_0 g\varsigma + \int_z^0 \rho g dz. \tag{6}$$

Substituting formula (6) in Eq. (1), and vertically integrating Eqs. (1) and (3) with the abovementioned boundary conditions for w (5.3) and (5.4), leads to the relation

$$f\vec{k}\times\vec{V} = -g\nabla\varsigma - \frac{g}{\rho_0 H}\int_{-H}^0 dz\int_z^0\nabla\rho dz + \frac{1}{\rho_0 H}\left(\vec{\tau}_s - \vec{\tau}_b\right) \tag{7}$$

$$\nabla\cdot\left(H\cdot\vec{V}\right) = 0 \tag{8}$$

in which $\vec{V}$ denotes the vertical average of the horizontal velocity vector. We introduce the stream function ψ from Eq. (8) as follows:

$$\vec{V} = \frac{1}{H}\vec{k}\times\nabla\psi = \left(\frac{1}{H}\int_{-H}^0 u dz, \frac{1}{H}\int_{-H}^0 \upsilon dz\right) \tag{9}$$

where $\vec{\tau}_b$ $(\tau_b{}^x, \tau_b{}^y)$ is the friction stress vector at the sea bottom H and satisfies the following formula:

$$\vec{\tau}_b = \rho_0 A_z\left(\frac{\partial\vec{v}}{\partial z}\right)_b = \rho_0 B\vec{V} = \rho_0 B\left(\frac{1}{H}\vec{k}\times\nabla\psi\right) \tag{10}$$

in which B is the bottom friction coefficient.

Substituting formula (9) for $\vec{V}$ in Eq. (7), we have

$$f\vec{k}\times\left(\frac{1}{H}\vec{k}\times\nabla\psi\right) = -g\nabla\varsigma - \frac{g}{\rho_0 H}\int_{-H}^0 dz\int_z^0\nabla\rho dz + \frac{1}{\rho_0 H}\left(\vec{\tau}_s - \vec{\tau}_b\right). \tag{7}'$$

After curl operating on Eq. (7)′ with formula (10), and then operating on the dot product $\vec{k}$ (the unit vertical vector), we obtain the following governing equation for the stream function ψ, which is obtained from the vorticity equation of the vertically integrated form of Eq. (1) (see also Yuan and Su, 1992; Yuan *et al*., 2004, 2005):

$$\underbrace{\frac{\partial}{\partial x}\left(\frac{B}{H^2}\frac{\partial\psi}{\partial x}\right) + \frac{\partial}{\partial y}\left(\frac{B}{H^2}\frac{\partial\psi}{\partial y}\right)}_{\text{I}} + \underbrace{\frac{f}{H^2}J(H,\psi)}_{\text{II}} + \frac{\beta}{H}\left(\frac{\partial\psi}{\partial x}\right) = \frac{1}{H}F \tag{11.1}$$

where

$$F = \frac{g}{\rho_0 H}J\left(H, \int_{-H}^0 z\rho dz\right) + \frac{1}{\rho_0}\left(\nabla\times\vec{\tau}_s\right)\cdot\vec{k} + \frac{1}{\rho_0 H}\left(\frac{\partial H}{\partial y}\tau_x - \frac{\partial H}{\partial y}\tau_y\right) \tag{12}$$

in which J is the Jacobian operator. On the right side of Eq. (11.1) or (12) the first term is due to the joint effect of the baroclinity and relief (JEBAR), and the second term is due to the effect of wind stress rotation (WSR), while the third term is due to the interaction between the wind stress and relief (IBWSR). Mertz and Wright (1992) emphasized that JEBAR may be regarded as a real forcing term when the density field is specified, as in a diagnostic calculation of the circulation. For the prognostic model, Kagimoto and Yamagata (1997) emphasized the importance of high resolution in capturing JEBAR, and Guo *et al*. (2003) also pointed out that the refinement of both topography and baroclinicity in the high-resolution model has naturally led to better representation of JEBAR. In this diagnostic calculation of the circulation, the terms JEBAR, IBWSR and WSR on the right side of Eq. (11.1) or (12) all are regarded as real forcing terms.

Equation (11.1) takes another form:

$$B\left(\frac{\partial^2\psi}{\partial x^2}+\frac{\partial^2\psi}{\partial y^2}\right)+Q\frac{\partial\psi}{\partial x}+G\frac{\partial\psi}{\partial y}=HF \qquad (11.2)$$

in which

$$Q=\underbrace{\beta H}_{\mathrm{I}'}-\underbrace{f\frac{\partial H}{\partial y}}_{\mathrm{II}'}-\frac{2B}{H}\frac{\partial H}{\partial x} \qquad (11.3)$$

and

$$G=f\frac{\partial H}{\partial x}-\frac{2B}{H}\frac{\partial H}{\partial y}. \qquad (11.4)$$

The first and second terms on the right side of the Q formula (11.3) are terms due to the ß effect and the topography effect, respectively.

The governing Eq. (11.1) or (11.2) for the stream function ψ satisfies the boundary conditions in the following two cases:

(1) On the open boundary condition

$$-\frac{\partial\psi}{\partial y}=\frac{\tau_y}{f\rho_0}-\frac{g}{f\rho_0}\int_{-H}^{0}z\frac{\partial\rho}{\partial y}dz-\frac{H}{f\rho_0}\frac{\partial p_H}{\partial y} \qquad (13.1)$$

$$\frac{\partial\psi}{\partial x}=-\frac{\tau_x}{f\rho_0}+\frac{g}{f\rho_0}\int_{-H}^{0}z\frac{\partial\rho}{\partial x}dz+\frac{H}{f\rho_0}\frac{\partial p_H}{\partial x} \qquad (13.2)$$

where p_H is the anomaly of pressure at the sea bottom, and the first term on the right side of Eqs. (13.1) and (13.2) is due to the action of the wind stress, the second term on the right side is given by the dynamic method (the sea bottom H is accepted as reference level, see also Sarkisyan, 1977), and the third term on the right side is the revised term for the dynamic method and is the component of the volume transport vector due to the bottom current, which can be obtained from the observed current. Because direct current measurements are scarce, the third term on the right side of Eqs. (13.1) and (13.2) is ignored in this computation.

(2) On the solid boundary condition: the stream function $\psi = 0$

In particular, for the most simple case the observed wind field and ß effect are considered with the uniform density field and $B = 0$, and the topography effect has not been considered and is assumed to be flat, the governing Eq. (11.1) or (11.2) for the stream function ψ is reduced to the Sverdrup relation:

$$\beta\left(\frac{\partial\psi}{\partial x}\right)=\frac{1}{\rho_0}\left(\frac{\partial\tau_y}{\partial x}-\frac{\partial\tau_x}{\partial y}\right). \qquad (14)$$

The governing Eq. (11.1) or (11.2) for the stream function ψ can be solved numerically with the boundary conditions (13.1) and (13.2) or the closed boundary condition.

With a constant A_z, the analytic solution of the horizontal velocity components $\vec{v}\,(u, v)$ can be obtained from Eqs. (1) and (2) with the boundary conditions (5.1)–(5.4), and divided into four parts (see Yuan and He, 1982; Yuan *et al*., 1986; Yuan and Su, 1988, 1992) as follows:

$$u=u_\tau+u_G+u_B+u_I \qquad (15.1)$$

$$v=v_\tau+v_G+v_B+v_I \qquad (15.2)$$

where (u_τ, υ_τ) are the surface Ekman velocity components subject to the wind stress $\vec{\tau}$, (u_G, υ_G) are the geostrophic velocity components, (u_B, υ_B) are the bottom Ekman velocity components which are almost zero outside the bottom Ekman layer, and (u_I, υ_I) are the velocity components due to baroclinic viscous effects. By definition, (u_I, υ_I) is zero at the sea floor, and they are less in general, as can be seen from comparison of the magnitude of the geostrophic velocity components term (u_G, υ_G) in Eq. (15) (see the following discussion). The explicit forms of the components in Eqs. (15.1) and (15.2) refer to Yuan *et al*. (1986) or Yuan and Su (1988, 1992). If (u_I, υ_I) can be ignored from formulas (15.1) and (15.2), we rewrite formulas (15.1) and (15.2) as follows:

$$u=u_\tau+u_G+u_B \qquad (15.1)'$$

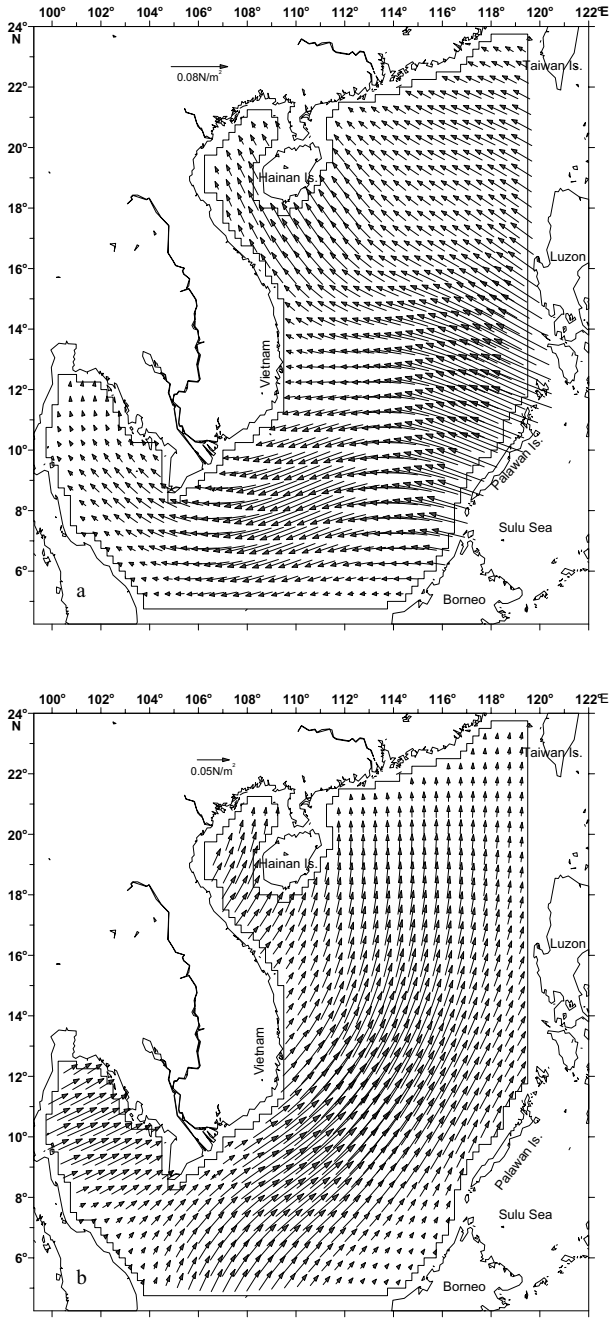

Fig. 2. Wind stress (N/m^2) distribution during (a) April 22–May 24, 1998; (b) June 12–July 6, 1998 (from Liao *et al.*, 2006).

$$v = v_\tau + v_G + v_B. \qquad (15.2)'$$

In formula (15) ($\partial\varsigma/\partial x$, $\partial\varsigma/\partial y$) can be obtained by the following relation between the sea surface elevation ς and stream function ψ, if the values of ψ are known. Substituting formula (10) in Eq. (7)′, we have

$$\frac{\partial\varsigma}{\partial x} = \frac{f}{gH}\frac{\partial\psi}{\partial x} - \frac{1}{\rho_0 H}\int_{-H}^{0}(H+z)\frac{\partial\rho}{\partial x}dz + \frac{\tau_x}{\rho_0 gH} + \frac{B}{gH^2}\frac{\partial\psi}{\partial y} \qquad (16.1)$$

$$\frac{\partial\varsigma}{\partial y} = \frac{f}{gH}\frac{\partial\psi}{\partial y} - \frac{1}{\rho_0 H}\int_{-H}^{0}(H+z)\frac{\partial\rho}{\partial y}dz + \frac{\tau_y}{\rho_0 gH} - \frac{B}{gH^2}\frac{\partial\psi}{\partial x}. \qquad (16.2)$$

Substituting formulas (16.1) and (16.2) in (15.1) and (15.2), we have another form of formulas (15.1) and (15.2) with the aid of stream function ψ, and their explicit forms of the components in another form of formulas (15.1) and (15.2) are given in Appendix.

Substituting formulas (15.1)′ and (15.2)′ of $\vec{v}(u, v)$ in Eq. (3) and after vertically integrating the continuity Eq. (3) with the boundary condition (5.3), we obtain the following approximate expression for the vertical component of velocity w outside the boundary layers (see also Sarkisyan, 1977):

$$w = \frac{1}{\rho_0 f} rot\vec{\tau}\cdot\vec{k} + \frac{\beta}{\rho_0 f^2}\tau_x + \frac{\beta z}{fH}\frac{\partial\psi}{\partial x} - \frac{zg\beta}{\rho_0 Hf^2}\cdot\int_{-H}^{0}(H+z)\frac{\partial\rho}{\partial x}dz - \frac{g\beta}{\rho_0 f^2}\int_{0}^{-z}(-z+\varsigma)\frac{\partial\rho}{\partial x}d\varsigma. \qquad (17)$$

The first term on right side of formula (17) is the vertical velocity component due to the action curl wind stress, namely, the effect of Ekman pumping, and the second term is the joint action between β effect and the wind stress $\vec{\tau}$. It is worth noting that the other terms on the right side of formula (17) depend on z, but the first and second terms are independent of z. In particular, when $\beta = 0$, the vertical component of velocity w is reduced to w_1 only due to the effect of Ekman pumping

$$w_1 = \frac{1}{\rho_0 f} rot\vec{\tau}\cdot\vec{k}. \qquad (17)'$$

3. Wind Data, Hydrographic Analysis and Altimeter Data

3.1 Wind data

The wind velocity field data with space resolution $2° \times 2°$ is extracted from National Centers Environmental Prediction (NCEP). The kriging method with linear variogram model is adopted to interpolate all data into the calculated grid of $0.25° \times 0.25°$. Next we also consider the ERS wind data in the same period; its horizontal resolution is $1° \times 1°$. Comparing the ERS wind data

with NCEP wind stress data in the same period, it is found that: 1) their directions of wind stress basically agree; 2) the maximum value of wind stress is about 0.04 N/m^2 for the ERS wind data but the maximum value of wind stress is about 0.08 N/m^2 for NCEP wind stress data. This means that the value of wind stress from ERS wind data is underestimated. Thus, NCEP wind data is used in this computation.

Figures 2(a) and 3(a) show the distributions of the wind stress and the curl wind stress in cruise 1, respectively. From Figs. 2(a) and 3(a) it is seen that in cruise 1, the SCS is dominated mainly by the southeasterly or easterly wind. The maximum value of wind stress is about 0.08 N/m^2 and is located southwest of Luzon Island, but the value of wind stress is less in the region east of Hainan Island. Figure 3(a) shows that the positive values of curl wind stress occur in the lower range of the region east of Vietnam, the middle part of the southern computed region, and part of the region northeast of Luzon, respectively. The negative value of curl wind stress occurs in the other part of the computed region.

In cruise 2, the northern SCS is dominated mainly by the southerly wind, and the other region of SCS is dominated mainly by southwesterly wind (Fig. 2(b)). As Fig. 2(b) shows, the maximum value of wind stress is about 0.07 N/m^2 and is located in the middle part of SCS. Figure 3(b) shows that the line with the zero value of curl wind stress is located generally from the southwest to the northeast in the computed region. The positive values of curl wind stress occur almost all in the region west of the line with the zero value of curl wind stress, except for Gulf of Thailand, and the negative values of curl wind stress occur almost all in the region east the line with the zero value of curl wind stress. The maximum positive value of curl wind stress is located east of Vietnam.

On May 23, 1998 was the date when the 1998 SCS Summer Monsoon was established (see He *et al.*, 1999).

3.2 Hydrographic analysis

For CTD data at the observed stations (see Fig. 1), we use also the kriging method with linear variogram model to interpolate all CTD data at observed stations into the calculated grid of 0.25° × 0.25°, and to obtain the horizontal distribution of water temperature and density. Owing to the limitation of space, only the horizontal distribution of water temperature and density at 200 levels is shown here. We discuss them below.

From the horizontal distribution of water temperature and density at 200 m (see Figs. 4(a) and (b)), the hydrographic character at the 200 m level has the following characteristics. (1) In the western part of the computed region there is warm, lower density water (called W1) in the region east of Vietnam, while colder, high density water (called C1) with a core exists southeast of

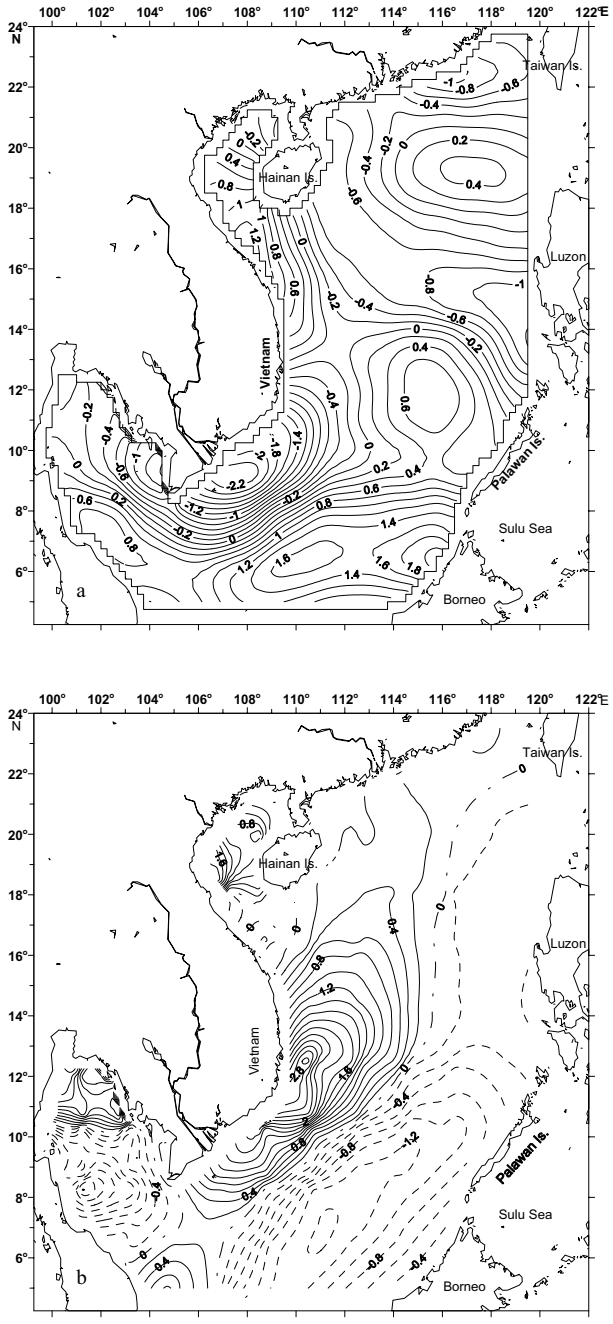

Fig. 3. Curl wind stress distribution (10^{-7} N/m^3) (a) April 22–May 24, 1998; (b) June 12–July 6, 1998. Solid (dashed) curves denote positive (negative) value (from Liao *et al.*, 2006).

the warm water W1. (2) In the region northeast of C1 and southwest of Luzon Island, there is warm, lower density water (called W2). (3) There is colder and higher density water (called C2) with two cores in the region west of Luzon strait and northwest of Luzon Island. (4) There is also the colder, higher density water (called C3) with a

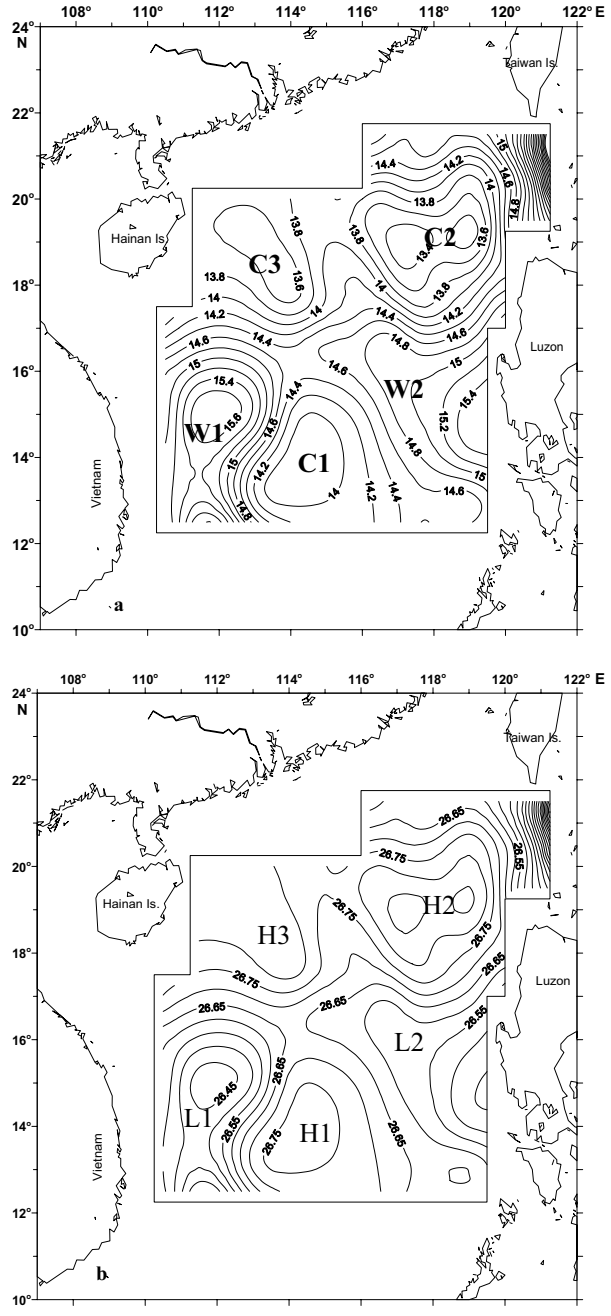

Fig. 4. Horizontal distribution of water temperature (°C) (a) and horizontal distribution of density (b) at 200 m levels in the computation region of the South China Sea during April 22–May 24, 1998.

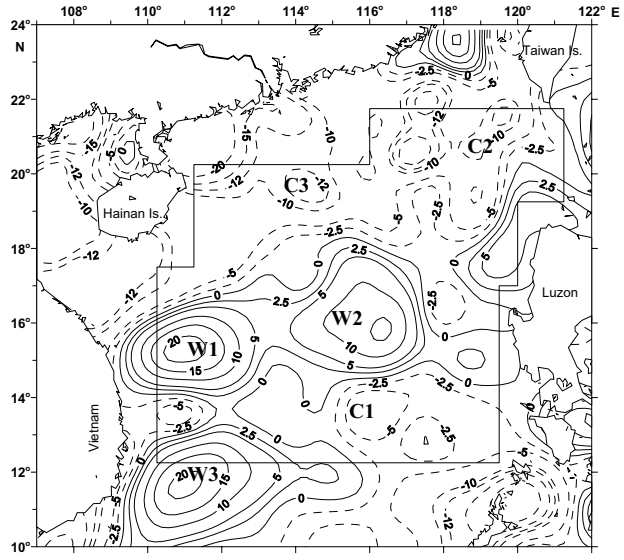

Fig. 5. Average values of sea surface height anomaly (SSHA) derived from TOPEX/Poseidon during the period from 29 April to 20 May. An anticyclonic warm eddy (W1), cyclonic cold eddy (C1), anticyclonic warm eddy (W2), and cyclonic eddy (C2) and so on are shown.

core in the region east of Hainan Island. In the layers above and below the 200 m level, such as the 500 m level the hydrographic character is similar to that at 200 m.

Finally, it is worth noting that the spatial interval between the CTD stations is larger in the area of colder and high density water C1, especially in the longitudinal direction. It is necessary to interpolate all CTD data with the aid of the kriging method at observed stations, as above. Of course, this results in some errors. However, comparison between Fig. 4 and Fig. 5, which display the average value of SSHA distribution derived from altimeter data T/P in the period from 29 April to 20 May, 1998, shows that they agree qualitatively, and the colder, high density water C1 does actually exist.

3.3 Altimeter data

The sea surface height anomaly (SSHA) distribution is extracted from the dataset compiled by the CLS Space Oceanographic Division of Toulouse, France. The dataset merges the Ocean Topography Experiment TOPEX/Poseidon, Jason-1, and European Remote Sensing Satellite ERS-1/2 along-track SSH measurements, and has a much improved capability of detecting mesoscale SSH signals. The CLS SSH dataset used in this study has a 7-day temporal resolution and a 1/3° × 1/3° spatial resolution. Figure 5 shows the average value of SSHA distribution derived from altimeter data, TOPEX/Poseidon, in the period from 29 April to 20 May, 1998. The dataset is corrected for instrumental errors, environment perturbations, the ocean wave influence, the tide influence and inverse barometer effect. The data processing can be found in detail in handbooks (see CLS, 2002). Next, Fig. 5 reflects the average value of SSHA distribution in the period from 29 April to 20 May, which can also eliminate the effects

Table 1. Numerical Experiments for selected parameter B and dynamical mechanism (the sign "√" in the table means that the corresponding terms are considered, and the sign "×" denotes that the corresponding terms have not been considered).

Experiment	Experiment name	B (ms^{-1})	Density field (ρ)	Topography (H)	Wind field (τ_s)	ß effect	JEBAR	IBWSR	WSC	Figure
Experiments for selected parameter B	Case 1-1	1×10^{-2}	√	√	√	√	√	√	√	Fig. 6(a)
	Case 1-2	5×10^{-2}	√	√	√	√	√	√	√	Fig. 6(b)
	Case 1-3	5×10^{-3}	√	√	√	√	√	√	√	Fig. 6(c)
	Case 1-4	1×10^{-3}	√	√	√	√	√	√	√	Fig. 6(d)
	Case 1-5	5×10^{-4}	√	√	√	√	√	√	√	Fig. 6(e)
Experiments for dynamical mechanism	Case 2	1×10^{-2}	√	√	×	√	√	×	×	Fig. 12(a)
	Case 3	1×10^{-2}	×	×	√	√	×	×	√	Fig. 12(b)
	Case 4	1×10^{-2}	×	√	√	√	×	√	√	Fig. 12(c)
	Case 5	1×10^{-2}	√	√	√	×	√	√	√	omitted
	Case 6	1×10^{-3}	×	×	√	√	×	×	√	Fig. 13(a)
	Case 7	5×10^{-4}	×	×	√	√	×	×	√	Fig. 13(b)
	Case 8	0	×	×	√	√	×	×	√	Fig. 13(c)

Fig. 6. Distribution of the stream function ψ (10^6 m^3/s) in SCS with the observed density and wind field, the actual bottom topography and ß effect during April 22–May 24, 1998, the bottom friction coefficient B is taken to be (a) 1×10^{-2} ms^{-1}; (b) 5×10^{-2} ms^{-1}; (c) 5×10^{-3} ms^{-1}; (d) 1×10^{-3} ms^{-1}; (e) 5×10^{-4} ms^{-1}.

due to higher frequency noise. From Fig. 5, the following results are obtained.

1) The circulation in the central SCS is dominated mainly by the anti-cyclonic gyre, and consists of the fol-

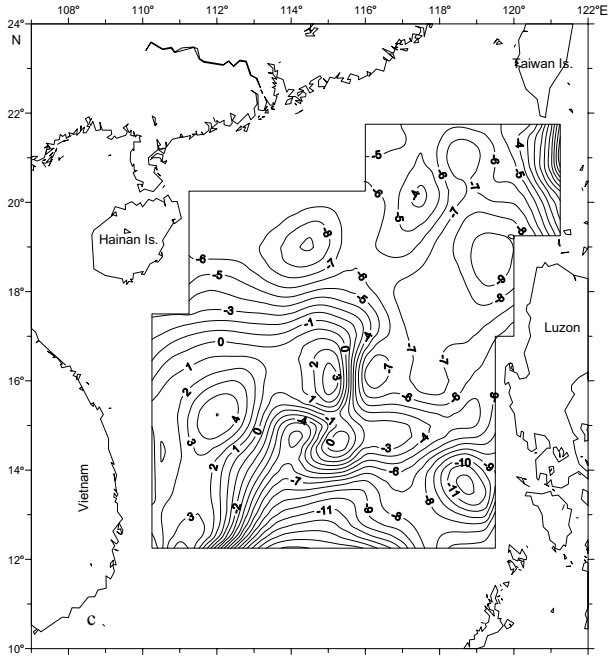

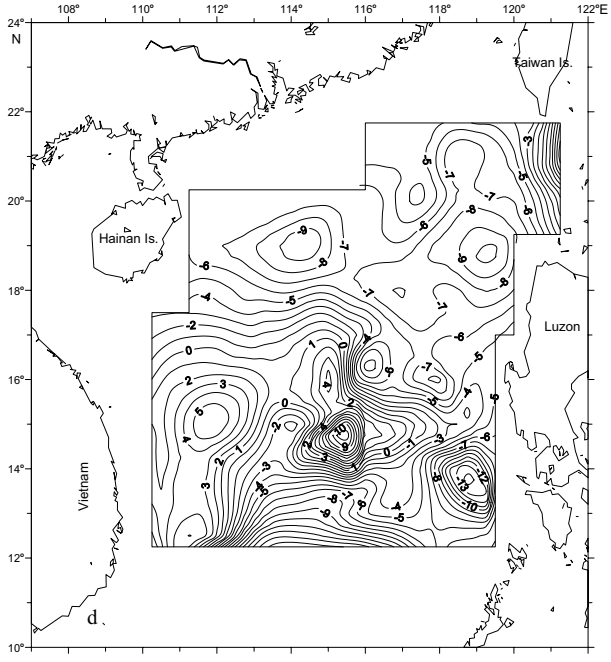

Fig. 6. (continued).

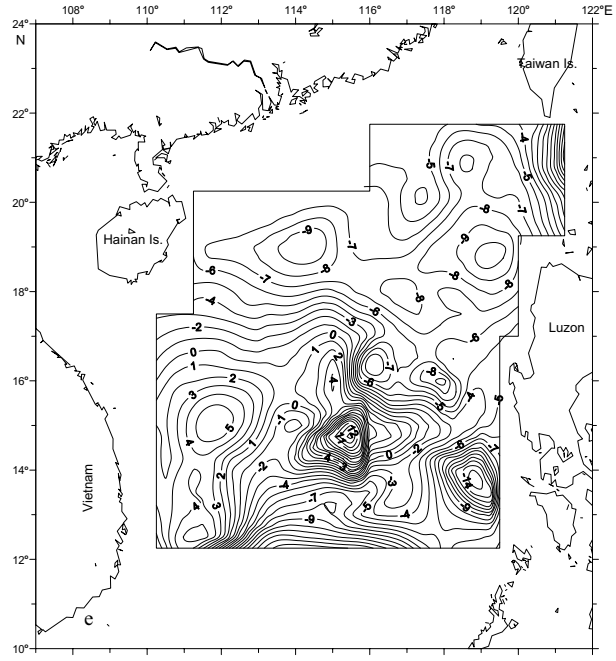

Fig. 6. (continued).

lowing the anti-cyclonic eddies. One is an anti-cyclonic eddy W1 and its center is about 15°N, 111°10′ E east of Vietnam. The center of the second anti-cyclonic eddy W2 is about 16°N, 116°E. The third anti-cyclonic eddy, W3, is located in the area south of W1 and its center is about 11°40′ N, 111°10′ E. 2) There is a cyclonic eddy C1 southeast of the anti-cyclonic eddies W1. 3) There is the cyclonic eddy C2 in the region west of Luzon strait and northwest of Luzon Island. The cyclonic eddy C3 exists in the region east of Hainan Island. The circulation in the northern SCS is mainly dominated by the cyclonic gyre, which consists of the above two cyclonic eddies C2 and C3.

4. Diagnostic Computation

The computed parameters are taken to be as follows. The computed meshes Δy = 27.8 km, $\Delta x = \Delta y \times \cos\theta$ = 27.65 km at 6.0°N, where θ is the latitude; $\beta = 2.19 \times 10^{-11}$ s^{-1}m^{-1}; when θ = 17.0°, $f_0 = 4.264 \times 10^{-5}$ s^{-1}. For the vertical kinematic eddy coefficient A_z, Yuan *et al.* (1986, 1992) experimented with different values of A_z, viz., 10, 50, 100 cm^2/s, and A_z = 100 cm^2/s was found to be more reasonable when comparing their computed results for different values of A_z with the observed currents, although the horizontal component of velocity vector $\vec{v} = (u, v)$ is not sensitive to different values of A_z. In this computation A_z = 100 cm^2/s is used. In the next place, the bottom friction coefficient B is taken to be 5×10^{-2}, 1×10^{-2} , 5×10^{-3}, 1×10^{-3} , 5×10^{-4} ms^{-1}. We discuss these values below.

4.1 Dependence of the stream function ψ on the bottom friction coefficient B

First of all, comparison of the magnitude of the first term (hereafter called term I) and second term (hereafter called term II) on the left side of Eq. (11.1) leads to γ= O

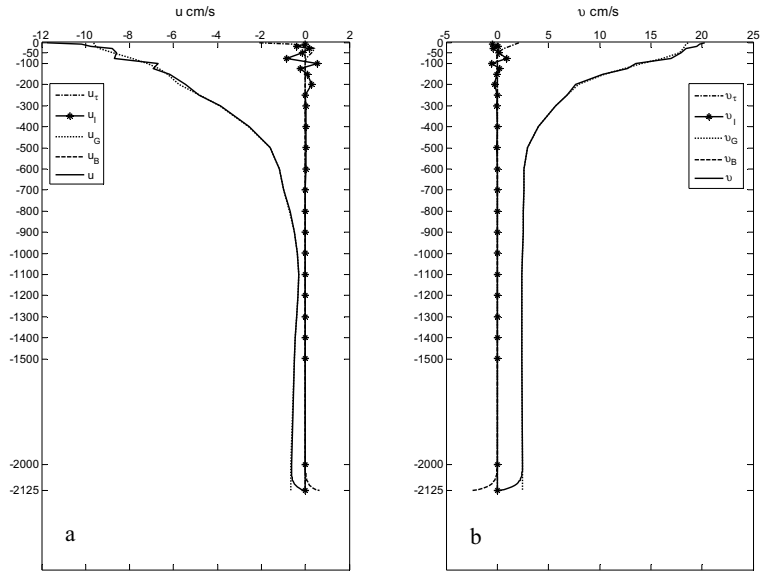

Fig. 7. Velocity profiles and their geostrophic and nongeostrophic components at computed point A (12.375°N, 110.375°E). (a) Eastward component u; (b) Northward component v (units: cm/s).

(term I) : O (term II) = B/f_0H_0. For $f_0 = 4.264 \times 10^{-5}$ s^{-1}, $H_0 = 2500$ m, we have $\gamma = 9.4$ sm^{-1} B. When the bottom friction coefficient B is taken to be 5×10^{-2}, 1×10^{-2} , 5×10^{-3}, 1×10^{-3} , 5×10^{-4} ms^{-1}, respectively, we obtain $\gamma \approx$ 0.5, 0.1, 0.05, 0.01, 0005, respectively. This means that γ = O (term I) : O (term II) is small for $B = 1 \times 10^{-2}$, 5×10^{-3}, 1×10^{-3} , 5×10^{-4} ms^{-1}.

We compute the following five cases (see Table 1): (1) Case 1-1: $B = 1 \times 10^{-2}$ ms^{-1}. The observed density and wind field are both considered and given in cruise 1, and the actual topography and ß effect are also both considered. The computed region is shown in Fig. 1. The boundary of the computed region is assumed to be open, corresponding to the open boundary (13.1) and (13.2); (2) Case 1-2. Case 1-2 is the same as Case 1-1 except that $B = 5 \times 10^{-2}$ ms^{-1}; (3) Case 1-3. Case 1-3 is the same as Case 1-1 except that $B = 5 \times 10^{-3}$ ms^{-1}; (4) Case 1-4. Case 1-4 is the same as Case 1-1 except that $B = 1 \times 10^{-3}$ ms^{-1}; (5) Case 1-5. Case 1-5 is the same as Case 1-1 except that $B = 5 \times 10^{-4}$ ms^{-1}.

For Case 1-1, from Fig. 6(a), the following results have been obtained. 1) The circulation in the central SCS is dominated mainly by the basin-scale anti-cyclonic gyre, and consists of the following three anti-cyclonic eddies: the anti-cyclonic eddy W1 east of Vietnam and anti-cyclonic eddy W2 in the area northeast of W1, and anti-cyclonic eddy W3 in the area south of W1. However, Fig. 6(a) only shows a part of anti-cyclonic eddy W3 due to the limitation of the computation region. A cyclonic eddy C1 exists in the area southeast of anti-cyclonic eddy W1. 2) The circulation in the northern SCS is mainly dominated by the basin-scale cyclonic gyre, which consists of the following two cyclonic eddies: a cyclonic eddy C2 in the region west of Luzon strait and northwest of Luzon Island, and a cyclonic eddy C3 in the region east of Hainan Island. Comparison of the hydrographic structure (Fig. 4) and Fig. 5 with the distribution of stream functions ψ in Case 1-1 (Fig. 6(a)) shows they agree qualitatively.

For Case 1-2 (see Fig. 6(b)), comparing Fig. 6(a) with Fig. 6(b), they are very different from each other. This is because the bottom friction coefficient B is taken to be greater.

For Case 1-3 (Fig. 6(c)), comparing Fig. 6(a) with Fig. 6(c), they agree basically and qualitatively, with only some quantitative changes. For example, a small cyclonic eddy exists northeast of anti-cyclonic eddy W2 for $B = 5 \times 10^{-3}$ ms^{-1} (Fig. 6(c)), which does not quite seem to coincide with the observed fact (see Figs. 4 and 5). But it does not appear for Case 1-1 (see Fig. 6(a)).

For Case 1-4 (Fig. 6(d)) and Case 1-5 (Fig. 6(e)), γ varies from 0.01 to .0005, namely, γ declines, hence Eq. (11.1) becomes a singular perturbation equation. Comparing Fig. 6(a) with Figs. 6(d) and (e), they agree qualitatively, but they are some quantitative differences. For example, when B decreases from 1×10^{-3} ms^{-1} (Fig. 6(d)) to 5×10^{-4} ms^{-1} (Fig. 6(e)), 1) the strength of anti-cyclonic eddy W2 and the cyclonic eddy in the most southwestern part of the computed region become increasingly strong, which does not seem to be reasonable. 2) There is a cyclonic eddy with two cores northeast of anti-cyclonic eddy W2 for $B = 1 \times 10^{-3}$ and 5×10^{-4} ms^{-1} (Figs. 6(d) and (e)), which does not seem to agree with the observed

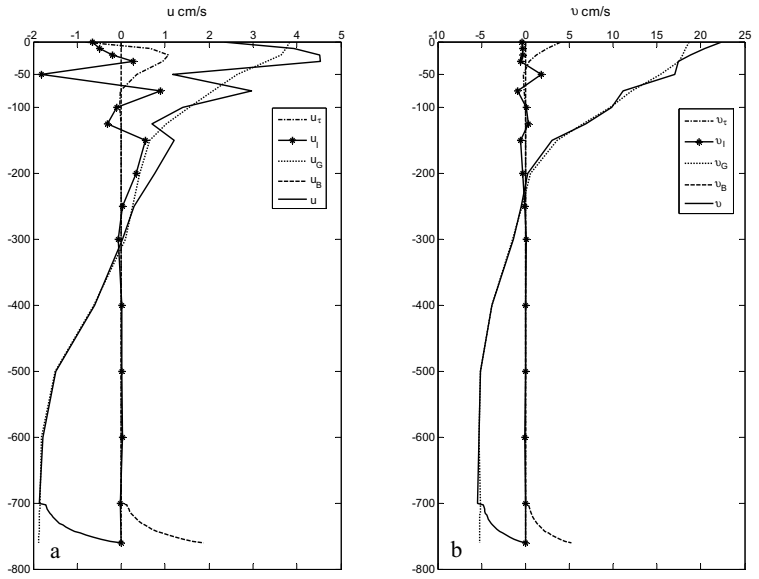

Fig. 8. Velocity profiles and their geostrophic and nongeostrophic components at computed point B (15.125°N, 110.625°E). (a) Eastward component *u*; (b) Northward component *v* (units: cm/s).

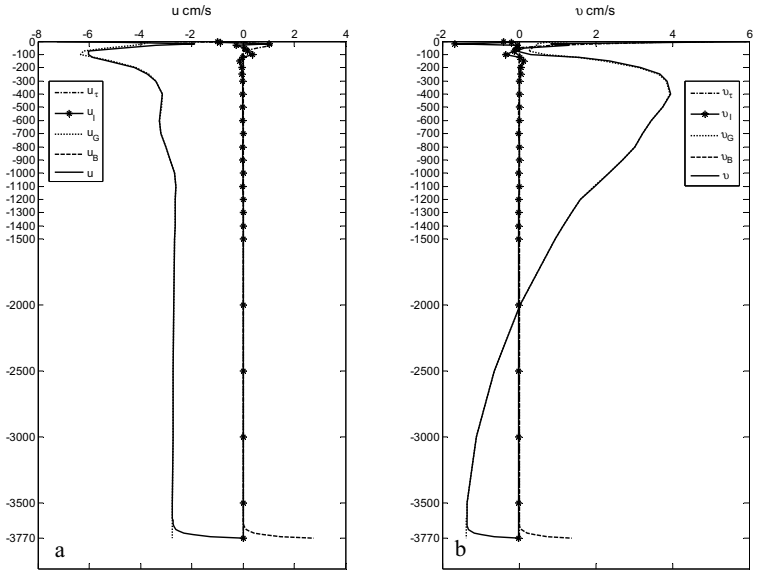

Fig. 9. Velocity profiles and their geostrophic and nongeostrophic components at computed point C (15.125°N, 114.375°E). (a) Eastward component *u*; (b) Northward component *v* (units: cm/s).

fact (see Figs. 4 and 5). This shows that the bottom friction coefficient B is taken to be too small for Case 1-4 (Fig. 6(d)) and Case 1-5 (Fig. 6(e)), which leads results that are not in agreement with observations (see Figs. 4 and 5).

From the above discussion, B is taken to be 1×10^{-2} ms^{-1} as a reasonable value. In this computation $B = 1 \times 10^{-2}$ ms^{-1} is used.

4.2 Velocity profiles of geostrophic and nongeostrophic components

To compare the geostrophic component of the horizontal velocity vector with the nongeostrophic components of the horizontal velocity vector, we compute four components of the horizontal velocity vector $\vec{v} = (u, \upsilon)$ from formulas (15.1) and (15.2) for five computed points A (12.375°N, 110.375°E); B (15.125°N, 110.625°E); C

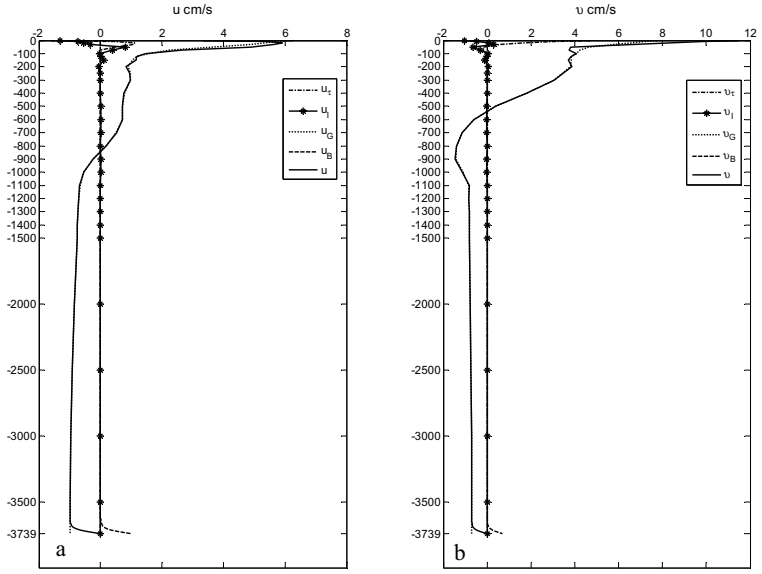

Fig. 10. Velocity profiles and their geostrophic and nongeostrophic components at computed point D (19.375°N, 119.125°E). (a) Eastward component u; (b) Northward component v (units: cm/s).

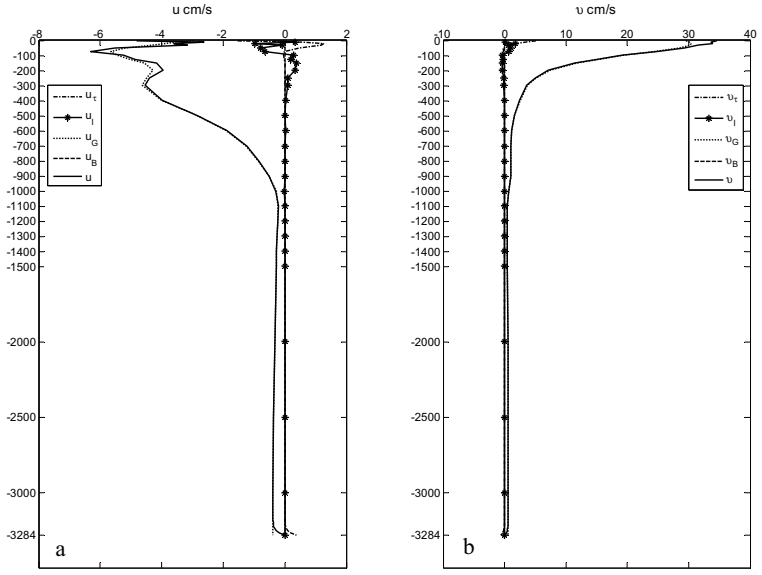

Fig. 11. Velocity profiles and their geostrophic and nongeostrophic components at computed point E (19.625°N, 120.625°E). (a) Eastward component u; (b) Northward component v (units: cm/s).

(15.125°N, 114.375°E); D (19.375°N, 119.125°E); E (19.625°N, 120.625°E).

The computed point A is located at the most southwestern computed point in the computed region, and is also located at the position of the northward coastal jet east of Vietnam (see below). From Fig. 7, all nongeostrophic components (u_τ, υ_τ), (u_I, υ_I) and (u_B, υ_B) are less than the geostrophic velocity components (u_G, υ_G) outside the bottom boundary layers. This means that the horizontal component of velocity vector $\vec{v} = (u, \upsilon)$ is almost geostrophic outside the bottom boundary layers at the computed points A.

The computed point B is located at the position of the northward coastal jet east of the coast of Vietnam (see as below). From Fig. 8, for the longshore velocity component (υ), all nongeostrophic components υ_τ, υ_I and υ_B

are less than the geostrophic velocity components v_G outside the bottom boundary layers. This means that the longshore velocity component (v) is almost geostrophic outside the bottom boundary layer at the computed points B. For offshore velocity component (u), the nongeostrophic components u_τ and u_I are of the same order of magnitude as the geostrophic component u_G in the upper layer, although the offshore velocity component (u) is very much less than the longshore velocity component (v). In the other layers the offshore velocity component (u) is almost geostrophic outside the bottom boundary layer. This characteristic of the offshore velocity component (u) near the coastal is very similar to that near the coast in the East China Sea (see Yuan *et al.*, 1986).

The computed point C is located north of the cyclonic eddy C1 (see below), the computed point D is located in area of the cyclonic eddy C2 (see as below), and the computed point E is located in the Luzon Strait, where it is affected by the intruded Kuroshio. Figures 9, 10 and 11 clearly show that: 1) the horizontal component of velocity vector $\vec{v} = (u, v)$ is almost geostrophic outside the surface and bottom boundary layers at the computed points C, D and E; 2) comparing the order of magnitude of the geostrophic components with the velocity components (u_I, v_I), in general (u_I, v_I) are less at the computed points C, D and E. However, we still retain the velocity components (u_I, v_I) due to baroclinic viscous effects in formulas (15.1) and (15.2), namely, we compute the horizontal component of velocity vector $\vec{v} = (u, v)$ according to formulas (15.1) and (15.2) in the following computation.

5. Diagnostic Model Results

5.1 Dynamical mechanism from stream function analysis

To examine the dynamical mechanism that produces the basic pattern of circulation in the SCS, we compute the following cases (see Table 1): (1) Case 1-1: Case 1-1 refers to the above; (2) Case 2: Case 2 is the same as Case 1-1 except for no wind field, namely the wind stress vector (τ_s^x, τ_s^y) = (0,0); (3) Case 3: The observed wind field and ß effect are considered with the uniform density field, and the topography effect has not been considered and is assumed to be flat with a water depth of 2000 m. The boundary of the computed region is shown in Fig. 12(b), and the boundary condition is assumed to be a closed one, namely stream function $\psi = 0$ on the closed boundary; (4) Case 4: Case 4 is the same as Case 3 except for considering the actual topography. From Eq. (11.1) or (11.2), the stream function ψ is obtained numerically. Figures 12(a), (b) and (c) show the distribution of the stream function ψ from the numerically simulated solution of Eq. (11.1) or (11.2) for three Cases 2, 3 and 4, respectively.

For Case 1-1, from Fig. 6(a), the results have been discussed above. In Case 2 the wind field has not been considered (the wind stress vector (τ_s^x, τ_s^y) = (0, 0)), the distribution of the stream function ψ is obtained (see Fig. 12(a)). In Case 2, the terms IBWSR and WSR both equal zero on the right side of Eq. (11.1) or (11.2). Comparing Fig. 12(a) with Fig. 6(a), they agree basically; there are only small quantitative changes. For example, the ranges of anti-cyclonic eddies W1, W2 and W3 in Case 1-1 are larger than those in Case 2. It is seen from the above comparison that the JEBAR term is the most important dynamical mechanism.

If the topography effect has not been considered with the uniform density field, i.e., Case 3, the distribution of the stream function ψ is obtained (see Fig. 12(b)). In Case 3, two terms JEBAR and IBWSR on the right side of Eq. (11.1) or (11.2), both equal zero. From Fig. 12(b), the cyclonic gyre exists in the area northwest of Luzon Island. There are basin-scale anti-cyclonic and cyclonic gyres, respectively, in northern and southern SCS. In Case 4 (Fig. 12(c)), the topography effect has been considered, but the uniform density field is assumed. If the density field is uniform, the first term, the JEBAR, on the right side of Eq. (11.1) equals zero. Figure 12(c) shows there are basin-scale cyclonic, anti-cyclonic and cyclonic gyres, respectively, in the northern SCS, central SCS, and the area southwest of Palawan Island and northwest of Borneo Island. Comparison of Fig. 12(b) with Fig. 6(a) shows they are very different from each other. Comparing Fig. 12(c) with Fig. 6(a), they are quantitatively different from each other. However, Fig. 12(c) shows that the circulation in the northern SCS is dominated by the basin-scale cyclonic gyre and the circulation in the central SCS is dominated by the basin-scale anti-cyclonic gyre, which seems to be qualitatively close to Fig. 6(a), despite their quantitative differences. From the above comparisons, Fig. 6(a) seems to be closer to Fig. 12(c) than Fig. 12(b).

In order to understand the dynamical mechanism further, we discuss the following two problems:

1) ß effect. Case 5 is the same as Case 1-1 except for ß = 0 (see Table 1), the distribution of the stream function ψ for Case 5 (figure omitted) is similar to Fig. 6(a) (Case 1-1). This means that the ß effect is not very important in Eq. (11.1). To discuss this problem further, one should note that the term due to the ß effect and the term due to the topography effect occur in the first term (hereafter called term I′) and second term (hereafter called term II′) on the right side of formula (11.3), respectively. Let us analyze and estimate the order of magnitude O (term I′) and O (term II′) for the first and second terms on right sides of the formula (11.3). The computed result leads to O (term I′) : O (term II′) = O (ε) : O (1) (ε is the less order of magnitude) for 75.5% of all computed points. This

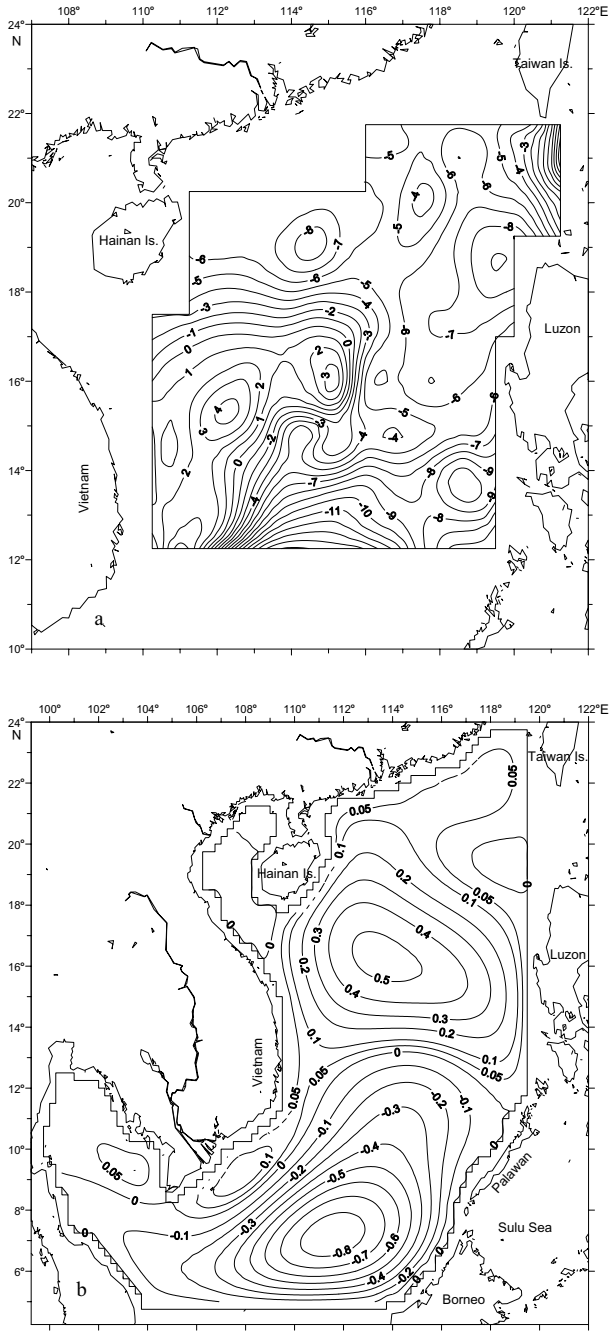

Fig. 12. Distribution of the stream function ψ (10^6 m^3/s) in SCS with $B = 1 \times 10^{-2}$ ms^{-1} (a) Case 2; (b) Uniform density field and flat topography with water depth of 2000 m (Case 3); (c) Actual bottom topography with uniform density field.

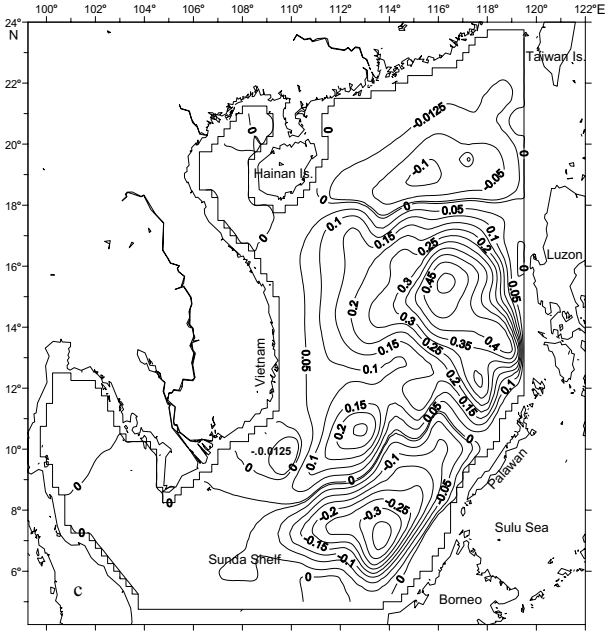

Fig. 12. (continued).

shows that the order of magnitude O (term II′) is greater than that of magnitude O (term I′) at most computed points, i.e., the topography effect is more important than the ß effect on the right side of formula (11.3).

2) Solution of the Sverdrup relation

For Case 3, when B decreases from 1×10^{-2} ms^{-1} to 5×10^{-4} ms^{-1}, i.e., γ is decreasing, Eq. (11.1) becomes a singular perturbation of a linear elliptic equation, and the boundary layer occurs at the western boundary of the computed region (Kevorkian and Cole, 1981), as shown in Figs. 13(a) and (b). Figures 13(a) and (b) show the distribution of the stream functions ψ for $B = 1 \times 10^{-3}$ ms^{-1} (Case 6) and 5×10^{-4} ms^{-1} (Case 7). Comparing Figs. 13(a) and (b) with Fig. 12(b), they agree qualitatively, but there are quantitative changes, namely when the bottom friction coefficient B decreases from 1×10^{-2} ms^{-1} to 5×10^{-4} ms^{-1}, the values of isograms of the stream function increase. In particular, when B tends zero, Eq. (11.1) for Case 3 reduces to the Sverdrup relation (14) (Case 8) and its solution is obtained, as shown in Fig. 13(c). If one compares Fig. 13(c) with Figs. 13(a) and (b), it is clear that: 1) the cyclonic gyre northwest of Luzon Island extends westward in Fig. 13(c); 2) Figs. 13(a) and (b) are both close to Fig. 13(c), while the values of isograms of the stream function increase in Fig. 13(c) because the bottom friction coefficient B equals zero. However, Fig. 13(c) is very different from Fig. 6(a). Hence, the Sverdrup relation cannot be satisfied for the dynamics of ocean currents in the SCS.

Now we summarize the above discussion of the dynamical mechanism, which produces the pattern of circulation in SCS. As stated above, the terms JEBAR, WSR and IBWSR are all regarded as real forcing terms when

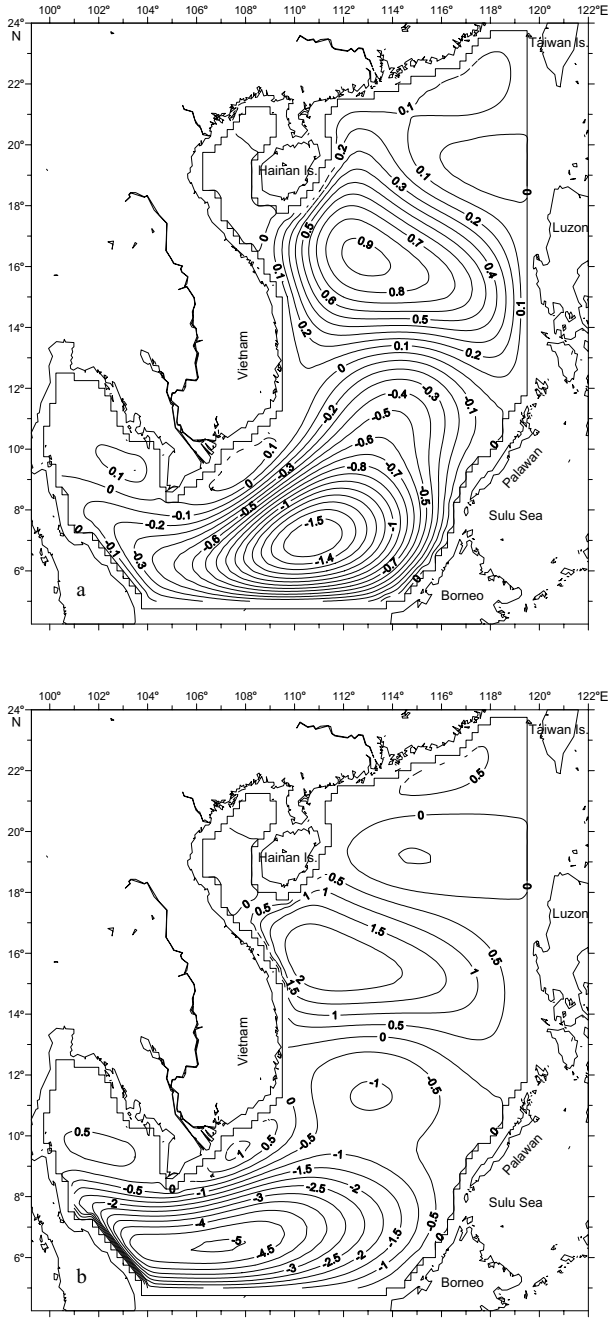

Fig. 13. Distribution of the stream function ψ (10^6 m^3/s) in SCS with uniform density field and flat topography with water depth of 2000 m (a) $B = 1 \times 10^{-3}$ ms^{-1}; (b) $B = 5 \times 10^{-4}$ ms^{-1}; (c) $B = 0$, Sverdrup relation.

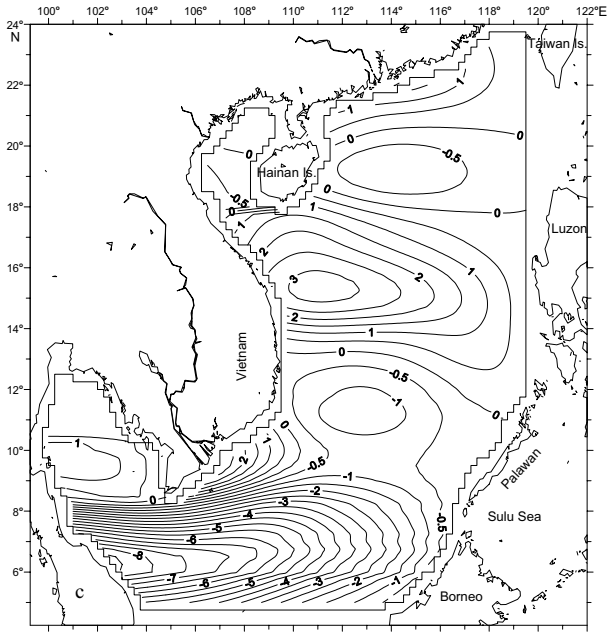

Fig. 13. (continued).

the density field is specified, as in a diagnostic calculation of the circulation (Mertz and Wright, 1992). It can be seen from the above comparison of Case 1-1 (Fig. 6(a)) with Cases 2, 3 and 4 (Figs. 12(a), (b) and (c)) that the most important dynamical mechanism is due to the joint effect of the baroclinity and relief (JEBAR). The second dynamical mechanism is due to the interaction between the wind stress and relief (IBWSR) under the southeasterly wind, as Yuan *et al*. (2004, 2005) also pointed out. Next, it is clear that: 1) the topography effect is more important than the ß effect; 2) for the specific and most simple Case 8, the Sverdrup relation cannot be satisfied for the dynamics of ocean currents in the SCS.

5.2 Horizontalvelocity field

When the density and wind fields are both given and the stream function ψ is obtained as shown in Fig. 6(a), the analytic solution of the horizontal velocity component $\vec{v}(u, \upsilon)$ for Eqs. (1)–(3) is also obtained from formulas (15.1) and (15.2). Figures 14(a)–(d) show the horizontal distribution of velocity at the 20 m, 100 m, 200 m and 500 m levels, respectively, in the SCS with the observed density field, ß effect and the actual bottom topography during April 22–May 24, 1998. From Figs. 14(a)–(d), the following major results are discussed.

5.2.1 Circulation system above 300 m levels in SCS

5.2.1.1 Circulation system in the northern SCS

From Figs. 14(a)–(c), most of the intruded Kuroshio does not intrude deeply into the SCS and the pathway of most of the Kuroshio passes by. However, part of the Kuroshio intrudes westward above 300 m levels. This shows that the Kuroshio intrusion weakens in cruise 1. Figures 14(a)–(c) show that this intruded westward flow is narrowly confined to the continental slope south of China above 300 m levels and does not appear to follow the western boundary throughout. Immediately to the

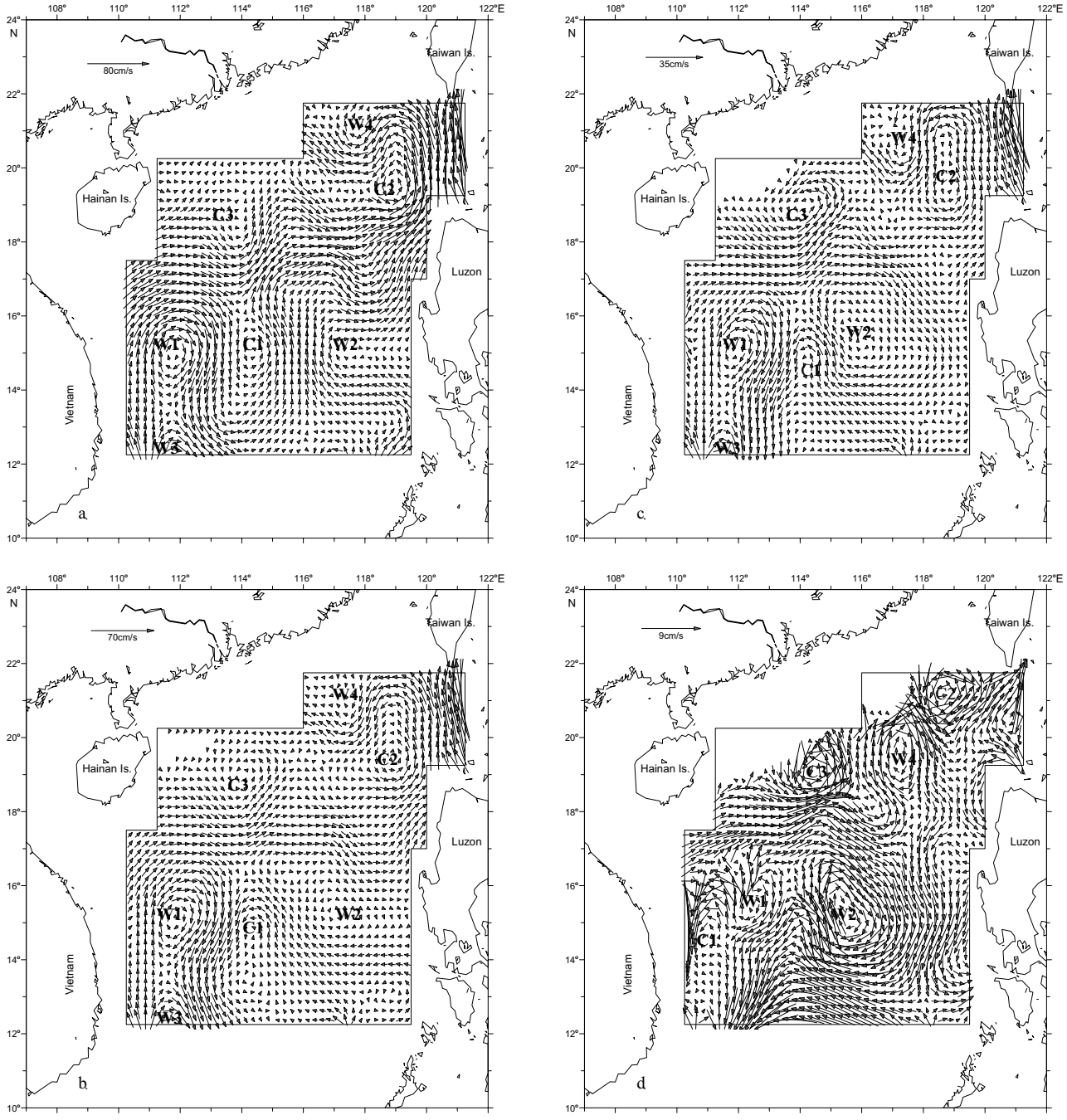

Fig. 14. Horizontal distribution of velocity (cm/s) at (a) 20 m level; (b) 100 m level; (c) 200 m level; (d) 500 m level from numerical solution of the diagnostic model with the observed density field, ß effect and the actual bottom topography in SCS during April 22–May 24, 1998.

south is an oppositely directed current, i.e., a northward coastal jet (see below) above 300 m levels. Comparing Figs. 14(a)–(c) with figures 10(a)–(c) in Qu *et al*. (2000), which show the geostrophic flow at 100 m computed from the dynamic height distribution (relative to 400 db), it is found that Figs. 14(a)–(c) is similar to figures 10(a)–(c) in Qu *et al*. (2000) in the Kuroshio intrusion from Luzon Strait, despite their differences in other regions. This indicates that the above computed results support the viewpoint of Qu *et al*. (2000), as pointed out in the Introduction.

From Figs. 14(a)–(c) show that circulation in the

northern SCS is dominated mainly by the basin-scale cyclonic gyre, which consists of the following two cyclonic eddies. One is a cold and cyclonic eddy C2 located in the area west of Luzon strait and northwest of Luzon Island. From the horizontal distribution of water temperature at 200 m levels (Fig. 4(a)), it is located from 18°~21°30′ N and 116°~119°E. Figures 14(a)–(c) show that its core is located near (19°30′ N, 119°E). Another is a cold and cyclonic eddy C3 and this is located in the area east of Hainan Island, its core being located near (19°N, 114°E). This reveals that the northern SCS is dominated mainly by the basin-scale cyclonic gyre above 300 m levels. Next, there is the anti-cyclonic eddy W4 with a smaller scale that exists northwest of cyclonic eddy C2 (Figs. 14(a)–(c)).

Figures 14(b) and (c) show that there is southwestward flow west of the cyclonic eddy C2 except at the surface. This southwestward flow may be the Dongsha Current, which was named by Su (1998, 2004). The Dongsha Current shown in Figs. 14(b) and (c) is only a part of the basin-scale cyclonic gyre in the northern SCS.

Finally, we explain the possible causes for the above weak basin-scale circulation, and there are two points to be noted: 1) As pointed out above, the third term on the right side of the open boundary condition (13.1) and (13.2) is ignored in this computation, i.e., the bottom current at the open boundary is ignored, while this bottom current probably contribute to the basin-scale circulation but is probably missed in this computation; 2) the open boundary condition on the Luzon Strait is most important among all open boundaries. As pointed out by Chu and Li (2000), in the spring and summer the Kuroshio weakens drastically through the Luzon Strait intrusion, and this probably results in weak basin-scale circulation.

5.2.1.2 Circulation system in the central SCS

In the central SCS there are the following the anti-cyclonic eddies. One is an anti-cyclonic eddy W1 and its center is located about (15°N, 111°50′ E) east of Vietnam. Another anti-cyclonic eddy W3 is shown only in part due to the limitation of the computation region (see Figs. 14(a)–(c)). Next, an anti-cyclonic eddy W2 exists, and its center is located at about (15°15′ N, 117°30′ E) at 20 m levels (Fig. 14(a)), (15°15′ N, 117°05′ E) at 100 m levels (Fig. 14(b)), and (15°15′ N, 116°E) at 200 m levels (Fig. 14(c)). The above variability reveals that its position moves westward from the surface to 200 m levels.

Figures 14(a)–(c) show that the anti-cyclonic eddies W1, W2 and W3 form the basin-scale anti-cyclonic gyre in the central SCS. Next, there is a cyclonic cold eddy C1 southeast of the anti-cyclonic eddy W1 in the central SCS.

5.2.1.3 Northward coastal jet

A stronger northward coastal jet is present at the western boundary near the coast of Vietnam at depths above the 300 m level, and separates anti-cyclonically from the western coast at about 17°15′ N to the northeast and then the east (see Figs. 14(a)–(c)). Immediately to the north is an oppositely directed current, i.e., the southeastward flow, as above. About 17°15′ N it branches into the following two parts: part of it turns anti-cyclonically to flow southward between the anti-cyclonic eddy W1 and a cyclonic eddy C1, and then it flows southward through the southern boundary of the computed region (see Figs. 14(a)–(c)). Another part joins with a southeastward flow from the north, and then continues to flow to the east to become the eastward jet (see Figs. 14(a)–(c)) (Wang *et al*., 2006). From Figs. 14(a)–(c), a northward coastal jet is a western part of the anti-cyclonic gyre.

Comparing Figs. 14(a)–(c) with Figs. 4, 5 and 6(a) it is found that the distribution of cyclonic and anti-cyclonic eddies agrees basically and qualitatively. In particular, the distributions of cyclonic circulation gyre and the anti-cyclonic gyre in Figs. 14(a)–(c) are similar to those in Fig. 6(a), respectively. However, there are quantitative changes between them, such as the sizes and positions of these eddies, which are different. This is because they have different physical senses for Figs. 4, 5, 6(a) and 14(a)–(c). For example, Fig. 4 reflects only the horizontal distribution of water temperature and density at 200 m level; Fig. 5 reflects only the geostrophic velocity components at the surface; Fig. 6(a) shows the distribution of the stream function, but Fig. 14(a) reflects the sum of geostrophic and nongeostrophic velocity components in the surface layer, while Figs. 14(b) and (c) reflects approximately the geostrophic velocity components at the 100 m and 200 m levels, respectively.

5.2.2 Circulation system below 300 m levels in SCS

5.2.2.1 Circulation system in the northern SCS

Figure 14(d) shows the horizontal distribution of velocity at the 500 m level. Figure 14(d) shows that the pathway of the Kuroshio bypasses the SCS at the 500 m level near the Luzon Strait, where its maximum velocity is 9.5 cm/s. In the northern SCS below 300 m level, the cold, cyclonic eddies C2 and C3 still exist, but their sizes and positions both vary. For example, a cyclonic eddy C2 moves northwestward, and its center is located at about (21°15′ N, 118°45′ E). Next, an anti-cyclonic eddy W4 moves southward and is located southwest of a cyclonic eddy C2, and its horizontal scale increases below 300 m. This shows that a cyclonic gyre below 300 m level is separated into two parts, viz., a cyclonic eddy C2 and a cyclonic eddy C3, by an anti-cyclonic eddy W4 in the northern SCS.

5.2.2.2 Circulation system in the central SCS

Comparing the circulation system below 300 m levels with that above 300 m, the following points should be noted. 1) A southward coastal flow exists instead of a northward coastal flow near the coast of Vietnam at levels below 300 m (see Fig. 14(d)). 2) A cyclonic eddy C4

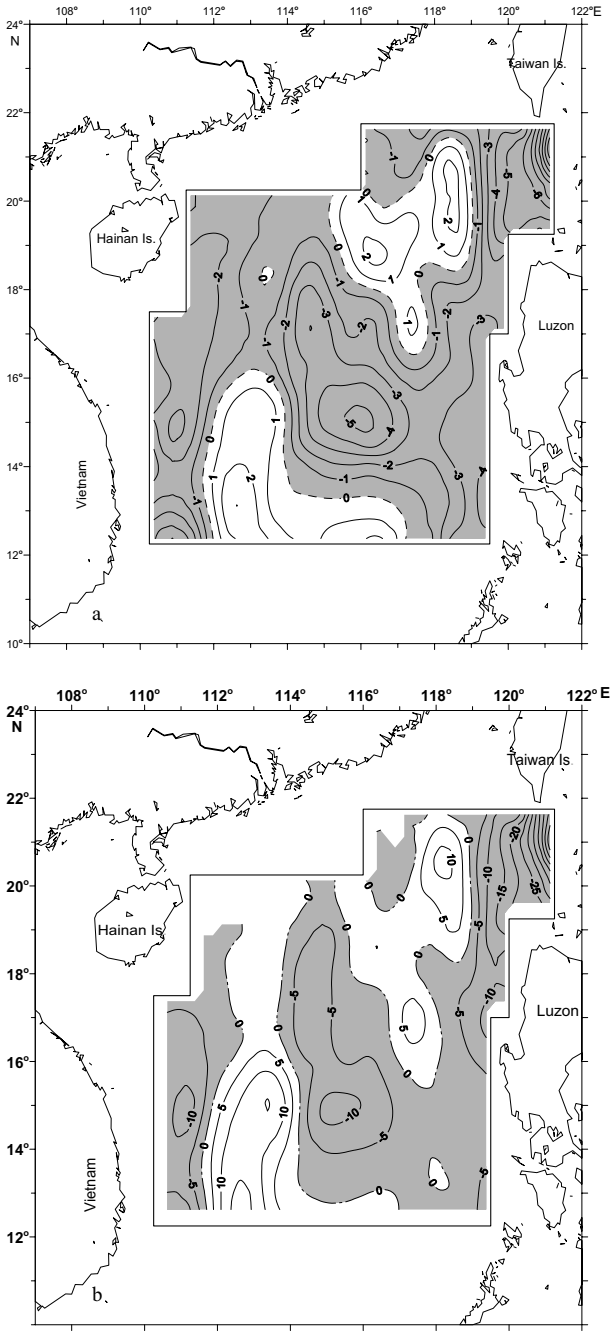

Fig. 15. Distribution of vertical component of velocity w (10^{-4} cm/s) in SCS during April 22–May 24, 1998 at (a) 30 m level, (b) 200 m level, (c) 600 m level. (Shaded parts: negative values; other parts: positive values.)

exists east of Vietnam instead of the position of the anti-cyclonic eddy W1, while the anti-cyclonic eddy W1 moves eastward, and its horizontal scale decreases. 3) The anti-cyclonic eddy W2 moves slightly westward. There is a southward flow in the area west of the Luzon Island

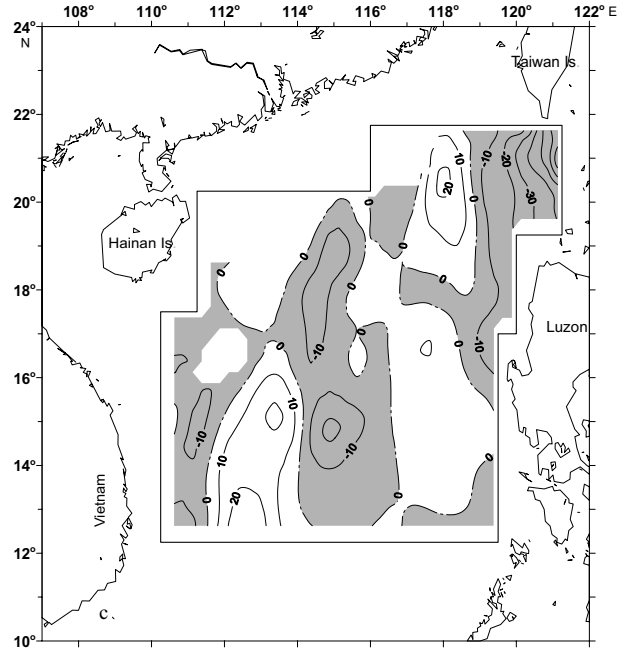

Fig. 15. (continued).

and east of W2 in the layer below 300 m level.

Comparing Fig. 14(d) with Figs. 14(b)–(c), there is an obvious change in the ranges and position of the basin-scale anti-cyclonic gyre below and above 300 m levels. The basin-scale anti-cyclonic gyre consists of the anti-cyclonic eddies W1, W2 and W4 and extends northward to near 20°N from the central SCS to the northern SCS below 300 m levels.

5.3 Vertical component of velocity w

We now discuss the distribution of vertical component of velocity (VCV) w in April 22–May 24 of 1998 as follows.

At the surface layer, such as the 30 m levels (see Fig. 15(a)), the positive w value occurs in the following areas (hereafter called area U): 1) It occurs in the middle part of the southern computed region and extends northward to about 16°5′ N, and its maximum value of positive w is greater than 2×10^{-4} cm/s; 2) it occurs in a part of the northeastern computed region and extends southward to about 16°30′. The negative w value occurs in the other region (hereafter called area D). Its maximum absolute value is greater than 1×10^{-3} cm/s in the Luzon Strait.

Comparing the distribution of w at the 30 m level (see Fig. 15(a)) with the distribution curl wind stress (see Fig. 4(a)), it is found that they agree basically in their change of signs. This shows that the dynamical cause of the vertical component of velocity w is mainly due to the

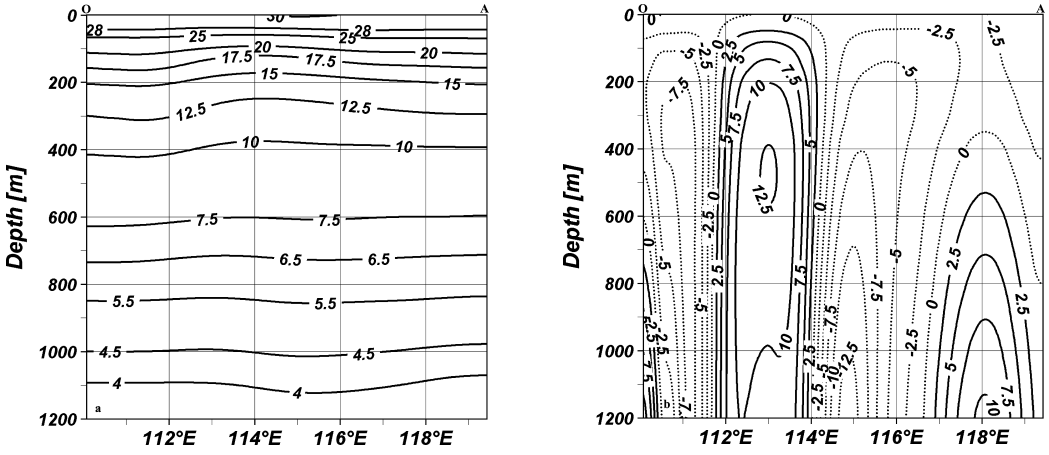

Fig. 16. Vertical distribution at section OA (at 14°N) in SCS during April 22–May 24, 1998 for (a) water temperature (°C), (b) vertical component of velocity w (10^{-4} cm/s).

effect of curl wind stress, i.e., due to the effect of Ekman pumping in the surface layer.

On the distribution of vertical component of velocity w in subsurface layer, such as 200 m levels (see Fig. 15(b)), the following results have been obtained. Comparing the distribution of w at the 200 m level (see Fig. 15(b)) with Fig. 15(a), there is some change in the areas U and D. For example, the U range of positive value of w changes and extends southward to 15°15′ N and its maximum value is greater than 5×10^{-3} cm/s. In general, the absolute value of w at the 200 m level is greater than that at the surface layer.

On the distribution of vertical component of velocity w in the middle layer, such as 600 m levels (see Fig. 15(c)), the following results have been found at 600 m levels. Comparing the distribution of vertical component of velocity w at 600 m levels (see Fig. 15(c)) with that at 30 and 200 m levels, the ranges of U and D all change. Further, recall that the first and second terms on the right side of formula (17) are independent of z, but the other terms depend on z. In general, their absolute value of w at the 600 m level is greater than that at the 30 m and 200 m levels from formula (17). On the dynamical cause for the distribution of vertical component of velocity w at 600 m levels, one finds that the joint action between the baroclinity and ß effect and the joint action between the barotropy and ß effect are both also important, besides the effect of Ekman pumping.

The distribution of vertical component of velocity w at 800 m levels is similar to that at 600 m levels.

Finally, we present a simple analysis of the following problem: does the upwelling take place off the Vietnamese coast during in April 22–May 24, 1998? Previous studies have shown that upwelling takes place off the Vietnamese coast in summer during the southwest monsoon. For example, see Wyrtki (1961), Huang *et al.* (1994), Xu *et al.* (1982), Kuo *et al.* (2000), Pohlmann (1987), and Shaw and Chao (1994) etc. Recently Xie *et al.* (2003) pointed out that in 1998, the cold filament and mid-summer cooling never took occurred, giving rise to a strong basin-wide surface warming.

Now we simply analyse the above problem. For example, we consider the colder and higher density water C1 to occur in the horizontal distribution of water temperature at 200 m level (see Fig. 4(a)), we take a zonal section OA, located at 14.0°N (see Figs. 1 and 16). Figure 16(a) shows the vertical distribution of water temperature at the section OA, and Fig. 16(b) shows the distribution of the vertical component of velocity w at the section OA. Figure 16(a) shows the warm water area W1, the colder water area C1 and a part of warm water area W2, respectively, from the west to the east. Comparing Fig. 16(b) with Fig. 16(a), the colder water area C1 generally corresponds to the positive w value, and its maximum positive w value is greater than 1.3×10^{-3} cm/s at 113°E and 500 m levels in the colder water area C1. It is noted that the center of the colder water is located at 114°E above 700 m levels, but it moves westward below 700 m; for example, it is at 112°E below 1000 m (see Fig. 16(a)). Next, there is also computational error, which comes from the interpolation of observed data and results in the difference of positions for the center of colder water and the maximum positive w value. From the above analysis, we cannot be sure that the upwelling may occur in the colder water area C1 yet, because we need support from other data, given the lack of data on oxygen concentration etc. in this area.

6. Variability of Circulation in the South China Sea during 1998

6.1 Circulation before and after the onset of the SCS summer monsoon in 1998

6.1.1 Northern SCS

In cruise 2 the location of observed hydrographic stations and the computation region are both different from those in cruise 1 (see Liao *et al.*, 2006). Figure 17(a) shows horizontal distribution of velocity at 200 m in cruise 2 (see Liao *et al.*, 2006). Now we present a simple discussion of the circulation system in the northern SCS during cruise 2. Figure 17(a) shows an anti-cyclonic warm eddy W4 west and northwest of Luzon Island. There is a cyclonic cold eddy C2, and its core is located at about 18°30′ N, 116°E, which is called the cyclonic cold eddy southwest of Dongsha (SCSIO, 1985).

Comparing the circulation in the northern SCS during cruise 1 with that during cruise 2, the ranges and positions of cold and warm eddies are different from each other. For example, a cyclonic cold eddy C2 moves southwestward in cruise 2 (see Figs. 14(c) and 17(a)). In particular, the range of the cyclonic gyre in the northern SCS is larger in cruise 1 than that in cruise 2.

6.1.2 Central SCS

As Fig. 17(a) shows, the anti-cyclonic warm eddy W3 southeast of Vietnam extends to the north about 13°45′ N in cruise 2 (see Liao *et al.*, 2006). However, an anti-cyclonic eddy W1 east of Vietnam, which occurs in cruise 1 (see Figs. 14(a)–(c)), disappears in cruise 2 (Fig. 17(a)). The cyclonic cold eddy C1 exists northeast of the anti-cyclonic eddy W3. Next, a warm eddy W2 exists northeast of the cyclonic cold eddy C1 in cruise 2. This shows that there are obvious changes in the range and position of the anti-cyclonic and cyclonic eddies in both cruises (see Liao *et al.*, 2006).

6.1.3 Variability of northward coastal jet

In cruise 2, a northward coastal jet is present at the western boundary near the coast of Vietnam at depths above 300 m levels, and separates anti-cyclonically from the coast to the east near 14°N, while immediately to the north there is an oppositely directed current, i.e., the southeastward flow. This then turns anti-cyclonically again and flows southeastward between the anti-cyclonic eddy W3 and a cyclonic eddy C1. Finally, it turns anti-cyclonically from the southeastward to the southward and flows southward through the southern boundary of the computed region (Fig. 17(a)). Comparing a northward coastal jet in cruise 1 with that in cruise 2, it is stronger in cruise 1 than that in cruise 2. Thus, it develops from the southern boundary of the computed region to about 17°15′ N in cruise 1. However, it develops from the southern boundary of the computed region to about 14°N in cruise 2. This shows that a northward coastal jet develops further northward in cruise 1 by about a distance of 3°15′ than that in cruise 2. Takano *et al.* (1998) also discussed this problem in terms of a numeral simulation, and obtained similar results to the above.

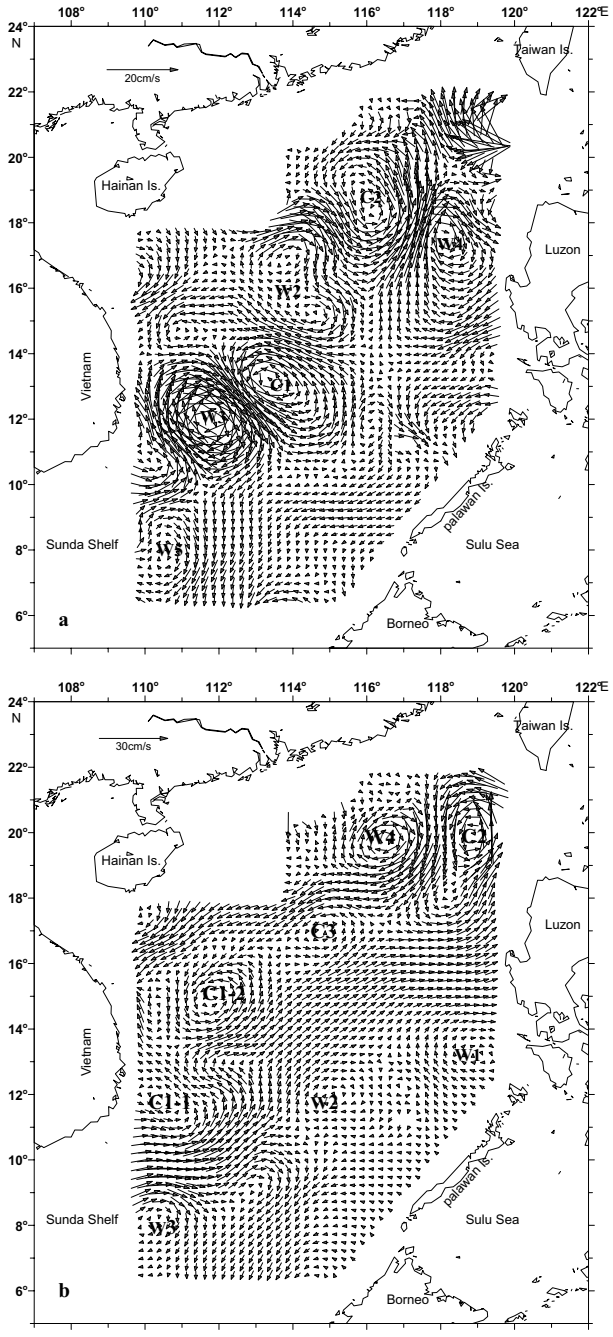

Fig. 17. Horizontal distribution of velocity (cm/s) in SCS at 200 m level during (a) June 12–July 6, 1998 (from Liao *et al.*, 2006), (b) November 28–December 27, 1998 (from Liao *et al.*, 2005).

6.1.4 Distribution of vertical component of velocity w

Comparing the distribution of the vertical component of velocity (VCV) *w* before and after the onset of the 1998 summer monsoon, one also sees obvious changes. For example, in the surface layer of cruise 1, the negative value of *w* occurs in the areas east of Vietnam, while the northeastern part of the computed region is mainly dominated by positive values of *w*. In the surface layer of cruise 2, the positive value *w* occurs in the areas east of Vietnam instead of the negative value, while the northeastern part of the computed region is mainly dominated by the negative values of *w* instead of the positive value. The above difference is mainly due to the effect of Ekman pumping with the different curl wind stress distribution in both cruises. In a similar manner, there are obvious changes in subsurface and deeper layers.

6.2 Circulation before the onset of 1998 summer monsoon and winter season

In November 28–December 27, 1998 the location of observed hydrographic stations and the computation region are both different from those in cruises 1 and 2 (see Liao *et al*., 2005). Figure 17(b) shows the horizontal distribution of velocity at 200 m level during November 28–December 27, 1998 (Liao *et al*., 2005). From Fig. 17(b), the northern SCS and a western part of central SCS are dominated mainly by the basin-scale cyclonic gyre, which consists of the cyclonic and cold eddies C1-1, C1-2 C2 and C3 during the winter of 1998. This indicates that the range of the cyclonic gyre is wider in winter when the northeast monsoon develops. Next, there are the anti-cyclonic eddies W4 west of C2, W2 east of the cyclonic eddy C1-1 and W1 southwest of Luzon Island. Comparing the circulation in the SCS during the winter of 1998 with that during cruise 1, the ranges and positions of the cyclonic and anti-cyclonic eddies are both obviously different for these two cruises.

Figure 17(b) also shows that a southward current, which has been called the Dongsha Current (Su, 1998, 2004), exists in the area between a cyclonic eddy C2 and the anti-cyclonic eddy W4 during the winter of 1998, and it is a part of the cyclonic gyre.

7. Conclusion

On the basis of hydrographic data obtained before the onset of 1998 summer monsoon (April 22–May 24) and the wind data from NCEP in the same cruise, the circulation in the SCS is computed by the three dimensional diagnostic model. The combination of sea surface height anomaly derived from TOPEX/Poseidon and numerical results provides a consistent circulation pattern for the SCS, the main circulation features of which can be summarized as follows:

(1) Circulation in the northern SCS

1. The Kuroshio intrusion weakens in cruise 1, and the pathway of most of the Kuroshio passes by. However, part of the Kuroshio intrudes westward above 300 m levels. This intruded westward flow is narrowly confined to the continental slope south of China above 300 m levels and does not appear to follow the western boundary throughout. Immediately to the south is an oppositely directed current, i.e., a northward coastal jet above 300 m levels. The above computed results support the viewpoint of Qu *et al*. (2000).

2. The circulation in the northern SCS is mainly dominated by the basin-scale cyclonic gyre, and consists of the cyclonic cold eddies C2 and C3 above 300 m levels. However, it is separated into two parts, viz., a cyclonic eddy C2 and a cyclonic eddy C3, by an anti-cyclonic eddy W4 in the northern SCS below 300 m levels.

3. The scope of the cyclonic gyre in the northern SCS is larger in cruise 1 than that in cruise 2. The scope of the basin-scale cyclonic gyre is wider in winter than that in cruise 1.

(2) Circulation system in the central SCS

The central SCS is dominated mainly by the basin-scale anti-cyclonic gyre, which consists of the three anti-cyclonic warm eddies W1, W2 and W3 above 300 m levels. However, there is an obvious change in the range and position of the basin-scale anti-cyclonic circulation above and below 300 m levels. Below 300 m levels the basin-scale anti-cyclonic gyre consists of the anti-cyclonic eddies W1, W2 and W4 and extends northward to near 20°N from the central SCS to the northern SCS. Next, there is a cyclonic cold eddy C1 southeast of the anti-cyclonic eddy W1 in the central SCS.

(3) A northward coastal jet is present at the western boundary near the coast of Vietnam at depths above the 300 m level, and separates anti-cyclonically from the western coast at about 17°15′ N to the northeast. It is stronger than that in cruise 2, and it develops further northward by about a distance of 3°15′ N than that in cruise 2.

(4) Comparing horizontal velocity profiles of geostrophic and nongeostrophic components, the currents are almost in geostrophic balance outside the surface and bottom boundary layers.

(5) The most important dynamical mechanism is due to the joint effect of the baroclinity and relief (JEBAR). The second dynamical mechanism is due to the interaction between the wind stress and relief (IBWSR) under the southeasterly wind. Next, it is clear that: 1) the topography effect is more important than the ß effect; 2) the Sverdrup relation cannot be satisfied for the dynamics of ocean currents in the SCS.

(6) Comparing the distribution of *w* in cruise 1 and cruise 2, there are obvious changes. For example in the surface

layer of cruise 1, the negative value *w* occurs in the areas east of Vietnam, while the northeastern part of the computed region is mainly dominated by the positive values of *w*. In the surface layer of cruise 2, the positive value *w* occurs in the areas east of Vietnam instead of the negative value, while the northeastern part of the computed region is mainly dominated by the negative values *w* instead of the positive value. The above difference is mainly due to effect of Ekman pumping with the different curl wind stress distribution in both cruises. In a similar manner, there are obvious changes in subsurface and deeper layers.

Acknowledgements

This work was supported by both the Key project of the National Natural Science Foundation of China (No. 40510073) and the State Basic Research Program of China (Grand No. G1999043805). The authors are very grateful to Dr. Tangdong Qu, IPRC, SOEST, University of Hawaii, for valuable comments and suggestions. The authors also deeply appreciate the anonymous reviewer for his valuable comments and suggestions.

Appendix

$$u_\tau = \frac{(\tau_x + \tau_y)[sh\eta\cos(2h+\eta) + sh(2h+\eta)\cos\eta]}{2\alpha\rho_0 A_z M} + \frac{(\tau_x - \tau_y)[ch(2h+\eta)\sin\eta + ch\eta\sin(2h+\eta)]}{2\alpha\rho_0 A_z M} \quad (A.1)$$

$$v_\tau = \frac{(\tau_y - \tau_x)[sh(2h+\eta)\cos\eta + sh\eta\cos(2h+\eta)]}{2\alpha\rho_0 A_z M} + \frac{(\tau_x + \tau_y)[sh(2h+\eta)\sin\eta + ch\eta\sin(2h+\eta)]}{2\alpha\rho_0 A_z M} \quad (A.2)$$

$$u_G = -\frac{\tau_y}{\rho_0 fH} + \frac{B}{fH^2}\frac{\partial\psi}{\partial x} - \frac{1}{H}\frac{\partial\psi}{\partial y} - \frac{g}{f\rho_0}\int_z^0 \frac{\partial\rho}{\partial y}dz' + \frac{g}{\rho_0 fH}\int_{-H}^0 (H+z)\frac{\partial\rho}{\partial y}dz \quad (A.3)$$

$$v_G = \frac{\tau_x}{\rho_0 fH} + \frac{B}{fH^2}\frac{\partial\psi}{\partial y} + \frac{1}{H}\frac{\partial\psi}{\partial x} + \frac{g}{f\rho_0}\int_z^0 \frac{\partial\rho}{\partial x}dz' - \frac{g}{\rho_0 fH}\int_{-H}^0 (H+z)\frac{\partial\rho}{\partial x}dz \quad (A.4)$$

$$u_B = \frac{2g(N_2 - N_3)}{fM}\cdot\left(\frac{\tau_x}{\rho_0 gH} + \frac{f}{gH}\frac{\partial\psi}{\partial x} + \frac{B}{gH^2}\frac{\partial\psi}{\partial y} - \frac{1}{\rho_0 H}\int_{-H}^0 z\frac{\partial\rho}{\partial x}dz\right) + \frac{2g(N_1 + N_4)}{fM}\cdot\left(\frac{\tau_y}{\rho_0 gH} + \frac{f}{gH}\frac{\partial\psi}{\partial y} - \frac{B}{gH^2}\frac{\partial\psi}{\partial x} - \frac{1}{\rho_0 H}\int_{-H}^0 z\frac{\partial\rho}{\partial y}dz\right) \quad (A.5)$$

$$v_B = \frac{2g(N_2 - N_3)}{fM}\cdot\left(\frac{\tau_y}{\rho_0 gH} + \frac{f}{gH}\frac{\partial\psi}{\partial y} - \frac{B}{gH^2}\frac{\partial\psi}{\partial x} - \frac{1}{\rho_0 H}\int_{-H}^0 z\frac{\partial\rho}{\partial y}dz\right) - \frac{2g(N_1 + N_4)}{fM}\cdot\left(\frac{\tau_x}{\rho_0 gH} + \frac{f}{gH}\frac{\partial\psi}{\partial x} + \frac{B}{gH^2}\frac{\partial\psi}{\partial y} - \frac{1}{\rho_0 H}\int_{-H}^0 z\frac{\partial\rho}{\partial x}dz\right) \quad (A.6)$$

$$u_I = \frac{2g(N_3 - N_2)}{f\rho_0 M}\cdot\int_{-H}^0\left[ch(h+\eta)\cos(h+\eta)\frac{\partial\rho}{\partial x} - sh(h+\eta)\sin(h+\eta)\frac{\partial\rho}{\partial y}\right]dz - \frac{2g(N_1 + N_4)}{f\rho_0 M}\cdot\int_{-H}^0\left[ch(h+\eta)\cos(h+\eta)\frac{\partial\rho}{\partial y} + sh(h+\eta)\sin(h+\eta)\frac{\partial\rho}{\partial x}\right]dz + \frac{g}{f\rho_0}\cdot\int_z^0\left[ch(\eta-\eta')\cos(\eta-\eta')\frac{\partial\rho}{\partial y} + sh(\eta-\eta')\sin(\eta-\eta')\frac{\partial\rho}{\partial x}\right]dz' \quad (A.7)$$

$$v_I = \frac{2g(N_3 - N_2)}{f\rho_0 M}$$
$$\cdot\int_{-H}^{0}\left[ch(h+\eta)\cos(h+\eta)\frac{\partial\rho}{\partial y} + sh(h+\eta)\sin(h+\eta)\frac{\partial\rho}{\partial x}\right]dz$$
$$+\frac{2g(N_1 + N_4)}{f\rho_0 M}$$
$$\cdot\int_{-H}^{0}\left[ch(h+\eta)\cos(h+\eta)\frac{\partial\rho}{\partial x} - sh(h+\eta)\sin(h+\eta)\frac{\partial\rho}{\partial y}\right]dz$$
$$-\frac{g}{f\rho_0}$$
$$\cdot\int_{z}^{0}\left[ch(\eta-\eta')\cos(\eta-\eta')\frac{\partial\rho}{\partial x} - sh(\eta-\eta')\sin(\eta-\eta')\frac{\partial\rho}{\partial y}\right]dz'. \quad (A.8)$$

In which

$$\left.\begin{aligned}&\alpha = \sqrt{\frac{f}{2A_z}},\ \ \eta = \alpha z,\ \ \eta' = \alpha z',\ \ h = \alpha H\\ &\text{and}\ \ M = \cos 2h + ch2h\end{aligned}\right\} \quad (A.9)$$

$$\left.\begin{aligned}N_1 &= \cosh chh\cos\eta\ ch\eta\\ N_2 &= \cosh chh\sin\eta\ sh\eta\\ N_3 &= \sinh shh\cos\eta\ ch\eta\\ N_4 &= \sinh shh\sin\eta\ sh\eta\end{aligned}\right\}. \quad (A.10)$$

References

Chu, P. and R. Li (2000): South China Sea isopycnal-surface circulation. *J. Phys. Oceanogr.*, **30**, 2419–2438.

Chu, P. C., N. L. Edmons and C. W. Fan (1999): Dynamical mechanisms for the South China Sea seasonal circulation and thermohaline variabilities. *J. Phys. Oceanogr.*, **29**, 2971–2989.

CLS (2002): SSALTO/DUACS User Handbooks, PP31.

Guo, X. Y., H. Hukuda, Y. Miyazawa and T. Yamagata (2003): A triply nested ocean model for simulating the Kuroshio—Roles of horizontal resolution on JEBAR. *J. Phys. Oceanogr.*, **33**, 146–169.

He, J. H., L. J. Wang and H. M. Xu (1999): Abrupt change in elements around 1998 SCS summer monsoon establishment with analysis of its onset. p. 30–33. In *Onset and Evolution of the South China Sea Monsoon and Its Interaction with the Ocean*, ed. by Y. Ding and C. Li, China Meteorological Press (in Chinese and English).

Hu, J., H. Kawamura, H. Hong and Y. Qi (2000): A review on the current in the South China Sea: Seasonal circulation, South China Sea Warm Current and Kuroshio intrusion. *J. Oceanogr.*, **56**, 607–624.

Huang, Q.-Z., W. Z. Wang, Y. S. Li and C. W. Li (1994): Current characteristics of the South China Sea. p. 39–47. In *Oceanography of China Seas*, ed. by D. Zhou, Y.-B. Liang and C. K. Tsebgm, Kluwer Academic Publishers.

Kagimoto, T. and T. Yamagata (1997): Seasonal transport variations of the Kuroshio: An OGCM simulation. *J. Phys. Oceanogr.*, **27**, 403–418.

Kevorkian, J. and J. D. Cole (1981): *Perturbation Methods in Applied Mathematics*. Springer-Verlag, New York Inc. Print, 558 pp.

Kuo, N. J., Q. Zheng and C. R. Ho (2000): Satellite observation of upwelling along the western coast of the South China Sea. *Remote Sens. Environme.*, **74**, 463–470.

Liao, G. H., Y. C. Yuan and X. H. Xu (2005): Diagnostic calculation of the circulation in the South China Sea during the winter of 1998. *Acta Oceanol. Sinica*, **27**(2), 8–17 (in Chinese with English abstract).

Liao, G. H., Y. C. Yuan and X. H. Xu (2006): Diagnostic calculation of the circulation in the South China Sea during the summer 1998. *J. Oceanogr.* (accepted).

Liu, Y. G., Y. C. Yuan, J. L. Su *et al.* (2000): Circulation in the South China Sea in summer 1998. *Chinese Science Bulletin*, **45**(18), 1648–1655.

Mertz, G. and D. G. Wright (1992): Interpretations of the JEBAR Term. *J. Phys. Oceanogr.*, **22**, 301–305.

Metzger, E. J. and H. E. Hurlburt (2001): The importance high horizontal resolution and accurate coastline geometry in modeling South China Sea inflow. *Geophys. Res. Lett.*, **28**(6), 1059–1062.

Pohlmann, T. A. (1987): Three-dimensional circulation model of the South China Sea. p. 245–268. In *Three-Dimensional Models of Marine and Estuarine Dynamics*, ed. by J. J. Nihoul and B. M. Jamart, Elsevier Sci., New York.

Qu, T. D. (2000): Upper-layer circulation in the South China Sea. *J. Phys. Oceanogr.*, **30**, 1450–1460.

Qu, T., H. Mitsudera and T. Yamagata (2000): Intrusion of the North Pacific waters into the South China Sea. *J. Geophys. Res.*, **105**, 6415–6424.

Qu, T. D., Y. Y. Kim, M. Yaremchuk, T. Tozuka, A. Ishida and T. Yamagata (2004): Can Luzon Strait transport play a role in conveying the impact of ENSO to the South China Sea? *J. Climate*, **17**, 3643–3656.

Sarkisyan, A. S. (1977): The diagnostic calculations of a large-scale oceanic circulation. p. 363–458. In *The Sea*, Vol. 6, ed. by E. D. Goldberg, I. N. Mccave, J. J. O'Brien *et al.*, A Wiley-Interscience Publication, New York.

Shaw, P. T. and S. Y. Chao (1994): Surface circulation in the South China Sea. *Deep-Sea Res. I*, **40**(11/12), 1663–1683.

South China Sea Institute of Oceanology (SCSIO), Chinese Academy of Science (1985): *Reports on the Integrated Investigation and Research in the South China Sea (II)*. Beijing Science Press, p. 204–231 (in Chinese).

Su, J. L. (1998): Circulation dynamics of the China Seas: north of 18°N. p. 483–506. In *The Sea*, Vol. 11, The Global Coastal Ocean: Regional Studies and Syntheses, ed. by A. R. Robinson and K. Brink, John Wiley.

Su, J. L. (2004): Overview of the South China Sea circulation and its influence of the coastal physical oceanography out-

side the pearl River Estuary. *Cont. Shelf Res*., **24**, 1745–1760.

Su, J. L., B. X. Guan and J. Z. Jiang (1990): *The Kuroshio. Part I. Physical Features. Oceanography and Marine Biology*. An Annual Review, **28**, 11–71.

Su, J. L., J. P. Xu, S. Q. Cai and O. Wang (1999): Gyres and eddies in the South China Sea. p. 66–72 or 272–279. In *Onset and Evolution of the South China Sea Monsoon and Its Interaction with the Ocean*, ed. by Y. H. Ding and C. Y. Li, China Meteorological Press (in Chinese and English).

Takano, K., A. Harashima and T. Namba (1998): A numerical simulation of the circulation in the South China Sea—Preliminary results. *Acta Oceanographica Taiwanica*, **37**(2), 165–186.

Wang, G. H., D. Chen and J. L. Su (2006): Generation and life cycle of the dipole in the South China Sea summer circulation. *J. Geophys. Res*., **111**, C06002, doi:10.1029/2005JC003314.

Wang, H. Q., Y. C. Yuan, W. B. Guan *et al*. (2004): Circulation in the South China Sea during summer 2000 as obtained from observation and a generalized topography-following ocean model. *J. Geophys. Res*., **10**, 1–12.

Wyrtki, K. (1961): Physical Oceanography of the Southeast Asia Waters. NAGA Report, **2**, 1–195.

Xie, S. P., Q. Xie and D. X. Wang (2003): Summer upwelling in the South China Sea and its role in regional climate variations. *J. Geophys. Res*., **108**(C8), 3261, doi:10.1029/2003JC001867.17-1-17-13.

Xu, X., Z. Qiu and H. Chen (1982): The general descriptions of the horizontal circulation in the South China Sea. p. 119–127. In *Proceedings of the 1980 of the Chinese Society of Marine Hydrology and Meteorology*, Sci. Press, Beijing.

Xue, H., F. Chai, N. Pettigrew and D. Xu (2004): Kuroshio intrusion and the circulation in the South China Sea. *J. Geophys. Res*., **109**, C02017, doi:10.1029/2002JC001724.

Yamagata, T. (2001a): The circulation and mechanism in the South China Sea (I). *Ocean Development News*, **29**(4), 2–8 (in Japanese).

Yamagata, T. (2001b): The circulation and mechanism in the South China Sea (II). *Ocean Development News*, **29**(5), 25–30 (in Japanese).

Yuan, Y. C. and K. R. He (1982): A computational method of three dimensional ocean current. *Acta Oceanol. Sinica*, **4**(6), 653–666 (in Chinese with English abstract).

Yuan, Y. C. and J. L. Su (1988): The calculation of Kuroshio current structure in the East China Sea—Early summer 1986. *Prog. Oceanogr*., **21**, 343–361.

Yuan, Y. C. and J. L. Su (1992): Numerical study of circulation over the continental shelf. p. 474–542. In *Numerical Computation of Physical Oceanography*, ed. by S. Feng and W. Sun, Henan Science and Technology Press (in Chinese).

Yuan, Y. C., J. L. Su and S. Y. Xia (1986): A diagnostic model of summer on the northwest of the East China Sea. *Prog. Oceanogr*., **17**, 163–176.

Yuan, Y. C., J. L. Su and Z. Q. Pan (1992): Volume and heat transports of the Kuroshio in the East China Sea in 1989. *La mer*, **30**, 251–262.

Yuan, Y. C., X. W. Bu, G. H. Liao *et al*. (2004): Diagnostic calculation of the upper-layer circulation in the South China Sea during the winter of 1998. *Acta Oceanol. Sinica*, **23**(2), 187–199.

Yuan, Y. C., Y. G. Liu, G. H. Liao, R. Y. Lou, J. L. Su and K. S. Wang (2005): Calculation of circulation in the South China Sea during summer of 2000 by the modified inverse method. *Acta Oceanol. Sinica*, **24**(1), 14–30.